Article

IL-27 elicits a cytotoxic CD8+ T cell program to enforce tumour control

Béatrice Bréart[1,2], Katherine Williams[1,2], Stellanie Krimm[1,2], Tiffany Wong[1], Brandon D. Kayser[1], Lifen Wang[1], Eric Cheng[1], Mayra Cruz Tleugabulova[1], Romain Bouziat[1], Tianshi Lu[1], Kobe Yuen[1], Natalie S. Firmino[1], Daniel D. Bravo[1], Juliette Roels[1], Atish Bhakta[1], Jack Bevers 3rd[1], Isabelle Lehoux[1], Alan Gutierrez[1], Yajun Chestnut[1], Joanna E. Klementowicz[1], Teresita L. Arenzana[1], Ilseyar Akhmetzyanova[1], Elizabeth Dixon[1], Min Chen[1], Kazi Tasneem[1], Rajbharan Yadav[1], Hartmut Koeppen[1], Soyoung A. Oh[1], Lélia Delamarre[1], Haochu Huang[1], Shion A. Lim[1], Gerald Nakamura[1], Jianyong Wang[1], Chan Gao[1], Racquel Corpuz[1], Sören Müller[1✉] & Nathaniel R. West[1✉]

Although cytotoxic CD8+ T lymphocytes (CTLs) are essential for anti-tumour immunity, they are frequently dysfunctional in tumours[1]. Cytokines that sustain CTL activity are attractive for cancer immunotherapy, but avoiding inflammatory toxicity remains a challenge for their clinical use[2]. Here we show that expression of a CTL signature is strongly associated with *IL27* expression in human and mouse tumours. In mice, IL-27 acts directly on tumour-specific CTLs to promote their persistence and effector function in the tumour microenvironment. Moreover, treatment with inducible IL-27 overexpression or a half-life-extended IL-27 protein in vivo is well tolerated, induces regression of established tumours, drives an enhanced cytotoxic program in anti-tumour CTLs and synergizes with PD-L1 blockade. In patients with cancer who were treated with anti-PD-1/PD-L1 therapy, high expression of IL-27 correlates with a favourable clinical response, and IL-27 supports human CTL function during chronic antigen stimulation ex vivo. Our data demonstrate that endogenous IL-27 is essential for anti-tumour immunity and that IL-27 receptor agonism can safely improve anti-tumour T cell responses alone or in combination with PD-L1 blockade.

CTLs are critical for anti-tumour immunity but have poor persistence and dysfunction in the harsh conditions of the tumour microenvironment (TME)[1]. While cancer immunotherapy (CIT) agents targeting CTLA4, PD-1 and PD-L1 have proven to be effective for stimulating protective T cell responses in diverse cancer types, most patients are unresponsive, suggesting that alternative or complementary therapeutic strategies are needed. Cytokines have been studied extensively as potential therapeutic agents due to their potent effects on T cell survival and function[2]. However, treatment with immunostimulatory cytokines such as IL-2, IL-12 and type I interferon (IFN) is constrained by poor tolerability due to immune-related toxicities. Moreover, cytokines exhibit rapid in vivo clearance, presenting a further challenge for clinical implementation[3]. Identifying cytokines with anti-tumour activity and a favourable safety profile is therefore a major challenge in the field of CIT. Here we reveal a strong association between IL-27 expression and CTL infiltration in human cancer and demonstrate that direct CTL-intrinsic IL-27 signalling is required for host-protective anti-tumour immunity in mice. Moreover, IL-27 pathway agonism enhances CTL responses and tumour control, without eliciting discernible toxicity.

Although the effects of IL-27 on CD4+ T cells are well characterized, including support of T helper type 1 (T_H1) and type 1 T regulatory ($T_{reg}1$) cell differentiation and inhibition of T_H2, T_H17 and T_{reg} cell differentiation[4,5], the impact of IL-27 on anti-tumour CTLs is not well understood. Previous reports described increased tumour growth in mice with IL-27

signalling deficiency[6,7], while attenuated tumour growth and improved CTL function has been observed in settings of increased IL-27 expression[8–10]. However, others have suggested that IL-27 may promote CTL dysfunction by inducing expression of co-inhibitory receptors such as PD-1[11,12]. Thus, the effects of IL-27 on tumour-specific CTLs require clarification.

IL-27 is correlated with CTLs in tumours

Despite their critical roles in regulating T cell responses, the specific cytokines required to support tumour-infiltrating CTLs remain unclear. To investigate the association between cytokines and CTL infiltration in human tumours, we first defined a CTL gene expression signature (CTLsig) composed of *CD8A* and components of cytotoxic machinery (*GZMA*, *GZMB*, *GZMH*, *GZMK*, *PRF1* and *NKG7*). We then correlated this signature with the expression of 201 cytokine-encoding genes in tumour samples from The Cancer Genome Atlas (TCGA), focusing initially on human cutaneous melanoma due to the immunogenicity and immunotherapy sensitivity of this cancer type[13,14] (Fig. 1a and Supplementary Table 1). We performed a similar comparison using published RNA-seq data[15] from 11 mouse tumour models representing a range of inflammatory phenotypes (Extended Data Fig. 1a). Expression of *IFNG* correlated strongly with CTLsig, consistent with its expression by activated CTLs. In both human and mouse tumours, CTLsig also correlated
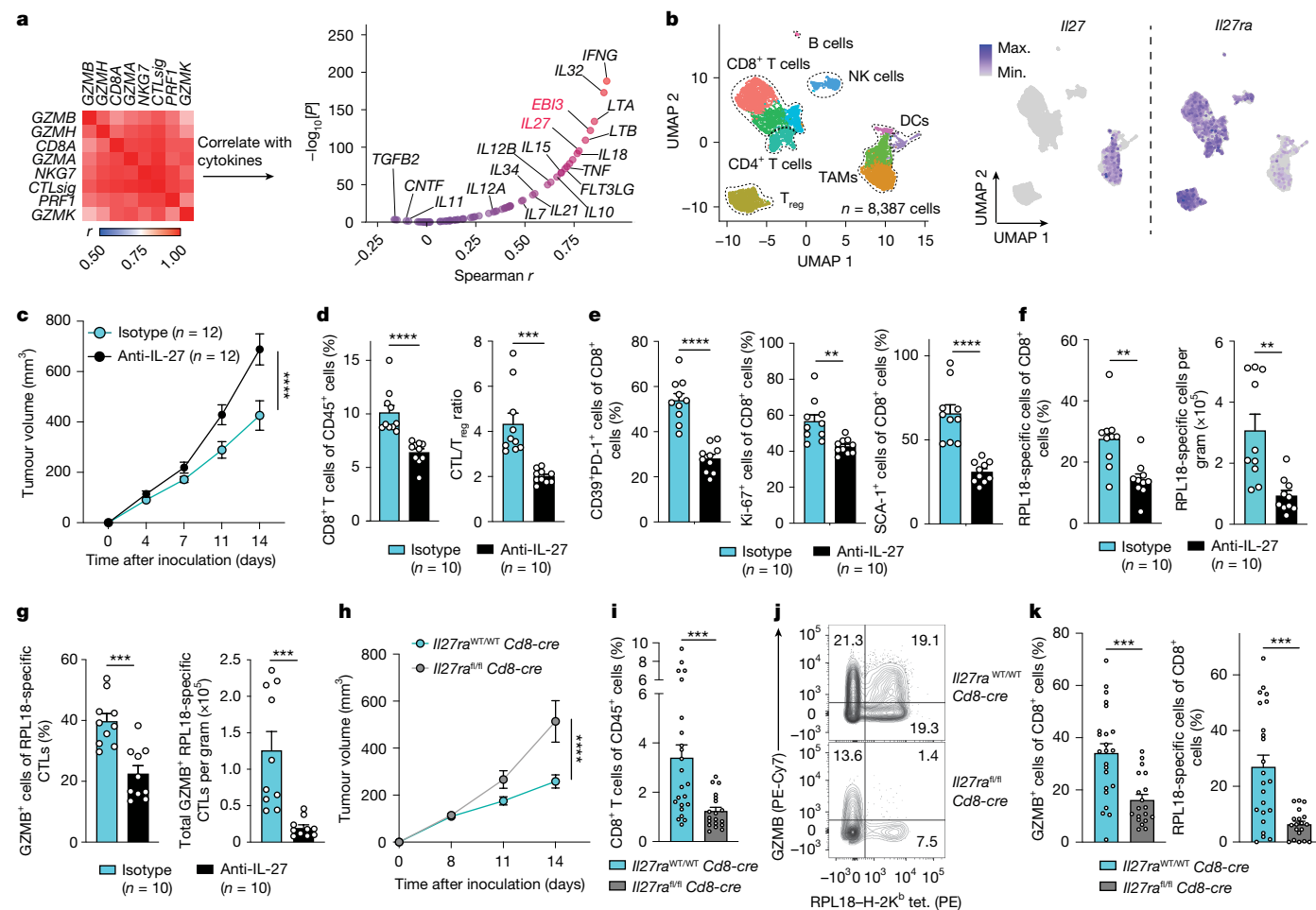
Fig. 1 | IL-27 correlates with CTLs in human tumours and is necessary for anti-tumour CTL responses in mice. a, Spearman correlation of cytokine and CTLsig expression in human melanomas (*n* = 470) from the TCGA-SKCM database. Data for 75 immunologically relevant cytokines are shown, while a broader analysis of 201 cytokines is provided in Supplementary Table 1. **b**, Uniform manifold approximation and projection (UMAP) visualization of CD45+ cells from MC38 tumours and the corresponding expression of *Il27* and *Il27ra*. TAMs, tumour-associated macrophages. **c–g**, Mice were inoculated with MC38 cells and treated with isotype control or anti-IL-27 antibodies. After 14 days, tumour-infiltrating T cells were analysed using flow cytometry. **c**, Tumour growth was compared using two-way analysis of variance (ANOVA) with Holm–Šidák multiple-comparison test. **d**, CTL frequencies (left) and CD8/ T_{reg} cell ratios (right). **e**, The expression of activation markers by CTLs. **f**, The frequency of RPL18-specific cells among CTLs (left) and their absolute abundance (right). **g**, GZMB expression in RPL18-specific CTLs (left), and the absolute numbers of GZMB+ RPL18-specific CTLs (right). **h–k**, *Il27ra*^fl/fl^*Cd8-cre* and *Il27ra*^WT/WT^ *Cd8-cre* mice were inoculated with MC38 cells. Then, 14 days after tumour inoculation, the tumours were analysed using flow cytometry. **h**, Tumour growth was compared using two-way ANOVA with Holm–Šidák multiple-comparison test. *n* = 25 (*Il27ra*^WT/WT^) and *n* = 23 (*Il27ra*^fl/fl^). **i–k**, Flow cytometry analysis of tumour-infiltrating CTLs. *n* = 23 (*Il27ra*^WT/WT^ and *n* = 19 (*Il27ra*^fl/fl^). **i**, Quantification of CD8+ T cells. **j**, Representative staining of GZMB and RPL18–H-2K^b^ tetramer (tet.). **k**, The frequencies of GZMB expression and RPL18-specific cells. For **d–g**, **i** and **k**, data are mean ± s.e.m. For **d–g**, **i** and **k**, statistical analysis was performed using two-sided Mann–Whitney *U*-tests; *P ≤ 0.05, **P ≤ 0.01, ***P ≤ 0.001, ****P ≤ 0.0001. For **c–g**, data are representative of two independent experiments. For **h–k**, data were combined from four independent experiments.

strongly with *IL27* and *EBI3*, which respectively encode the p28 and EBI3 subunits of the heterodimeric cytokine IL-27[16] (Fig. 1a and Extended Data Fig. 1a). To corroborate these findings, we correlated cytokine expression in human melanoma with a previously published effector T (T_{eff}) cell signature[17] and observed a similar association with *IL27* and *EBI3* (Spearman *r* > 0.75; Extended Data Fig. 1b). By contrast, *IL27* and *EBI3* were weakly associated with a published signature[17] of innate inflammatory response (Spearman *r* < 0.25; Extended Data Fig. 1c). A broader analysis of TCGA data revealed that *IL27* is associated with CTLsig across numerous solid tumour types (Extended Data Fig. 1d), demonstrating that this relationship is not unique to melanoma.

IL-27 is thought to be produced mainly by myeloid leukocytes[4]. Thus, to determine whether the IL-27–CTLsig association is driven primarily by the presence of activated myeloid cells, we correlated CTLsig with the myeloid-derived IL-27 family members *IL12A* and *IL23A*. In nearly all solid tumour types, CTLsig expression correlated more strongly

with *IL27* (median Spearman *r* = 0.56) than with either *IL12A* (median Spearman *r* = 0.28) or *IL23A* (median Spearman *r* = 0.19) (Extended Data Fig. 1d). Other cytokines that correlated closely with CTLsig were also correlated with *IL27* and *EBI3*, including the known IL-27-inducible genes *IL10* and *IL21*[18,19] (Extended Data Fig. 1e). Consistent with the close association between *IL27* and CTLsig, transcriptome-wide analysis of *IL27*-associated genes in diverse tumour types revealed enrichment of pathways related to T cell activation, cytokine signalling and antigen presentation (Extended Data Fig. 1f).

IL-27 is essential for anti-tumour CTLs

To elucidate the functional relationship between IL-27 and tumour-infiltrating CTLs, we conducted a series of in vivo studies using syngeneic mouse tumour models, starting with MC38. Like human melanoma, MC38 tumours have a high mutation load, elicit host-protective

T cell responses and are sensitive to checkpoint blockade immunotherapy[20–22]. Single-cell RNA-sequencing (scRNA-seq) analysis of MC38 tumour-infiltrating leukocytes (TILs) confirmed that *Il27* and *Ebi3* were co-expressed exclusively by myeloid cells, whereas co-expression of the IL-27 receptor components[23] IL-27RA (encoded by *Il27ra*) and gp130 (encoded by *Il6st*) was restricted largely to T and natural killer (NK) cells (Fig. 1b and Extended Data Fig. 2a). Using flow cytometry, we confirmed that T cells expressed IL-27RA in tumours and draining lymph nodes (dLNs), whereas no expression was detectable in myeloid cells (Extended Data Fig. 2b). Among members of the gp130/IL-6 cytokine family (which generally signal through STAT3), IL-27 is unusual in its ability to induce preferential activation of STAT1[24]. Indeed, compared with IL-6, we confirmed that IL-27 is a strong activator of STAT1 in mouse T cells, but induces STAT3 less effectively (Extended Data Fig. 2c,d).

We next compared the growth of MC38 tumours in wild-type (WT), *Il27ra*-knockout (KO) or *Ebi3*-KO mice and observed faster tumour growth in animals lacking IL-27 signalling (Extended Data Fig. 2e,h). To account for possible developmental phenotypes arising from constitutive IL-27 deficiency, we treated mice with an IL-27 neutralizing antibody (Extended Data Fig. 3a) and observed similarly increased tumour growth (Fig. 1c). In all settings, loss of IL-27 signalling significantly decreased CTL frequency and abundance in tumours (Fig. 1d and Extended Data Figs. 2f,g,i,j and 3b,c) but not in dLNs (Extended Data Fig. 2f,i). As IL-27 had relatively little effect on CD4+ T cell numbers, IL-27 deficiency was associated with a significantly reduced CD8/T$_{reg}$ cell ratio in tumours (Fig. 1d and Extended Data Figs. 2f,g,i,j and 3d).

Having shown that IL-27 sustains CTL abundance in tumours, we next evaluated tumour-infiltrating CTL phenotypes in the setting of IL-27 deficiency. IL-27 blockade or IL-27RA deficiency reduced the frequency of CD39+PD-1+ cells, a population that is enriched for tumour-reactivity and cytotoxic activity[25] (Fig. 1e and Extended Data Figs. 2k and 3e,f). Similarly, IL-27 deficiency caused reduced CTL proliferation (determined by Ki-67 expression) and low expression of effector molecules including the cytotoxicity mediator GZMB (Fig. 1e and Extended Data Figs. 2k,l and 3g). Loss of IL-27 signalling also attenuated expression of SCA-1 (encoded by *Ly6a*), a STAT1/3-inducible marker of T cells with progenitor-like properties[26] (Fig. 1e and Extended Data Fig. 2k). By contrast, loss of IL-27 signalling had little impact on CTLs in the dLN (Extended Data Fig. 3h). IL-27RA deficiency also impaired CTL responses to orthotopic E0771 mammary tumours, which are less responsive to immunotherapy than MC38[27], although tumour growth was less impacted in this system (Extended Data Fig. 4a–d). Consistent with the ability of IL-27 to promote T$_H$1 and T$_{reg}$1 cell differentiation[4,5], the effector function of CD4+ T cells in MC38 tumours (including expression of IFNγ and TNF) was reduced by IL-27 blockade (Extended Data Fig. 3i).

MC38 cells contain an MHC-I (H-2K^b)-restricted neo-antigen encoded by a point mutation in ribosomal protein L18 (encoded by *Rpl18*) that elicits an immunodominant CTL response, enabling us to identify definitively tumour-reactive T cells[28] (Extended Data Fig. 2m). In both the *Il27ra*-KO and IL-27 blockade settings, RPL18-specific CTLs (particularly those expressing GZMB) were significantly reduced in MC38 tumours, but not in the dLNs (Fig. 1f,g and Extended Data Figs. 2m and 3j,k). Overall, our data suggest that IL-27 is required for host-protective anti-tumour CTL responses.

IL-27 effects on CTLs are cell intrinsic

Next, to identify the critical source of IL-27 in tumour-bearing mice, we crossed *Il27*-floxed mice with animals expressing *LysM-cre* or *Clec9a-cre* to conditionally delete IL-27 from phagocytes or dendritic cells (DCs), respectively. Whereas IL-27 deficiency in phagocytes had only modest effects on anti-tumour CTLs (Extended Data Fig. 4e–g), deletion of IL-27 in DCs recapitulated the phenotype of *Il27ra*-KO mice (Extended Data Fig. 4h–j), demonstrating an essential role for DC-derived IL-27 in anti-tumour immunity.

To determine whether IL-27 affects CTLs through a cell-intrinsic mechanism, we first generated mixed WT:*Il27ra$^{-/-}$* chimeric mice by reconstituting sublethally irradiated CD45.1+ recipients with WT or *Il27ra$^{-/-}$* CD45.2+ bone marrow (Extended Data Fig. 2n). Under these competitive conditions, both *Il27ra*-KO and WT donor-derived T cells were detected at frequencies equal to those of host cells in the dLN, but donor-derived CTLs in MC38 tumours were markedly reduced in mice that received *Il27ra*-KO marrow. Similarly, the effector function of donor-derived IL-27RA-deficient CTLs and CD4+ T cells was attenuated in tumours (Extended Data Fig. 2n). Thus, although IL-27 can potentially act through multiple cell types including NK and CD4+ T cells[4,5,29] (Fig. 1b), it probably affects tumour-specific CTLs in a cell-intrinsic manner. To confirm this mechanism, we crossed *Il27ra*-floxed and *E8i-CD8a-cre* mice to ablate IL-27RA exclusively in CD8+ T cells[30]. Indeed, deletion of *Il27ra* in CTLs caused increased tumour growth (Fig. 1h), reduced the abundance of total and RPL18-specific CTLs in tumours, and reduced CTL expression of activation markers (Fig. 1i–k and Extended Data Fig. 4k). Thus, CTLs require direct IL-27 stimulation for sustained anti-tumour function.

IL-27R agonism enhances tumour control

We next investigated the effect of systemic IL-27 receptor (IL-27R) agonism in mice with established MC38 tumours (>150 mm³). As recombinant cytokines are cleared rapidly from circulation[3,31], we delivered IL-27-encoding (or empty control) plasmids to the liver using hydrodynamic tail vein (HTV) injection[32,33], resulting in high serum IL-27 concentrations (up to 1 µg ml^{-1}) that lasted for a week or more (Fig. 2a). Notably, IL-27R agonism induced complete tumour rejection in a majority of mice without causing overt toxicity (Fig. 2b–d). By contrast, overexpression of other IL-27 family members in healthy mice (including IL-6, IL-12 and IL-23) caused rapid weight loss and high levels of inflammatory cytokines in the serum (Extended Data Fig. 5a,b).

Consistent with previous reports[5,19,24], IL-27 induced significant transcriptional changes in CD4+ T cells from tumours and dLNs including increased expression of STAT/IFN-response genes, IL-12 receptor subunits, IL-21 and IFNγ (Extended Data Fig. 5c). IL-27 similarly increased expression of STAT1-inducible markers such as Ly6c, SCA-1 and PD-L1[26,34] in CTLs from tumours and dLNs (Fig. 2e). IL-27 increased CTLs in tumours without promoting T$_{reg}$ cell infiltration, leading to an increased CD8/T$_{reg}$ cell ratio (Fig. 2f). Owing to a reduction in T$_{reg}$ cell frequency, IL-27 also increased the CD8/T$_{reg}$ cell ratio in dLNs (Extended Data Fig. 5d). IL-27 induced high levels of Ki-67, CD39, GZMA and GZMB in CTLs, while cytokine expression was less affected (Fig. 2g,h and Extended Data Fig. 5e,f). CD8+ TILs from IL-27-treated mice displayed enhanced control of tumour cell proliferation ex vivo (Fig. 2i). Although the frequency of RPL18-specific cells among CTLs was not affected by IL-27R agonism, they showed increased expression of GZMB, SCA-1 and Ki-67, consistent with the broader CTL population (Extended Data Fig. 5g,h). Thus, in addition to the important role of endogenous IL-27 signalling, IL-27R agonism promotes vigorous anti-tumour CTL responses and improved tumour control.

We next evaluated IL-27R agonism in mice with E0771 mammary tumours or B16-F10 melanomas which, in contrast to MC38 tumours, are resistant to PD-1/PD-L1 blockade[27,35]. While E0771 elicits a robust CTL response, this is counterbalanced by a substantial T$_{reg}$ cell infiltrate. By contrast, B16-F10 tumours are poorly infiltrated by all T cell subsets (Extended Data Fig. 6a). Notably, transient IL-27R agonism in combination with sustained PD-L1 blockade induced regression of E0771 tumours and delayed growth of B16-F10 tumours (Extended Data Fig. 6b,c). Anti-PD-L1 single-agent therapy increased both tumour-infiltrating CTLs and T$_{reg}$ cells, resulting in no appreciable change in the CD8/T$_{reg}$ cell ratio (Extended Data Fig. 6d,e). By contrast, IL-27R agonism alone or in combination with anti-PD-L1 increased CTL abundance while reducing T$_{reg}$ cells, resulting in substantially increased
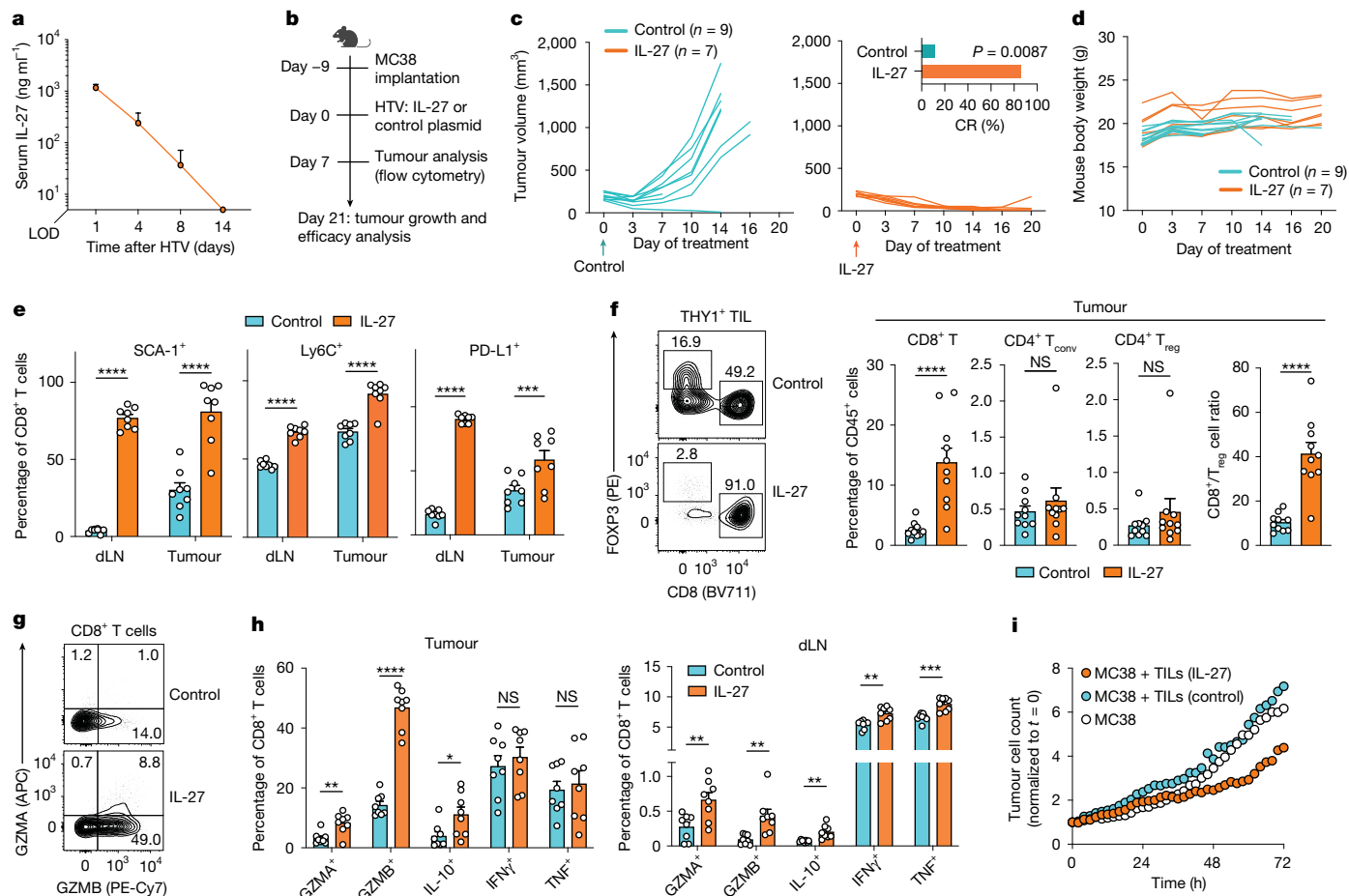
Fig. 2 | Inducible IL-27 overexpression promotes anti-tumour CTL response and tumour regression. a, The serum IL-27 concentration after HTV injection of IL-27-encoding plasmid in healthy C57BL/6J mice was measured using an enzyme-linked immunosorbent assay (ELISA). Data are mean ± s.e.m. from n = 3 mice per timepoint. LOD, limit of detection. **b**, The experimental approach for **c**–**i**. C57BL/6J mice were engrafted with MC38 cells. When tumours reached 150 mm³ (day 0), the mice were treated once with HTV injection of control or IL-27-encoding plasmid. The mouse icon was created using BioRender. **c**,**d**, The tumour volumes (**c**) and body weights (**d**) in IL-27-treated or control-treated mice. Complete response (CR) frequencies are indicated in **c**, compared using Fisher's exact tests. **e**, The frequency of STAT1/3-responsive markers in CTLs.

n = 8 per group. **f**, The frequencies of FOXP3⁻CD4⁺ conventional T (T_{conv}) cells, FOXP3⁺CD4⁺T_{reg} cells and CTLs among total CD45⁺ cells, and the corresponding CD8/T_{reg} cell ratios. n = 10 per group. **g**, Representative intracellular staining of GZMA and GZMB in tumour-infiltrating CTLs. **h**, Expression of granzymes and cytokines in CTLs after restimulation with PMA and ionomycin. n = 8 per group. **i**, Ex vivo control of MC38 cells by MC38-tumour-derived CTLs from mice treated with control or IL-27-encoding plasmids. Data are representative of two experiments with 5–7 tumours pooled per group. Data in **a**–**h** are representative of three independent experiments. For **e**,**f** and **h**, data are mean ± s.e.m. Statistical analysis was performed using two-sided Mann–Whitney U-tests (**f** and **h**) or two-way ANOVA (**e**). NS, not significant (P > 0.05).

CD8/T_{reg} cell ratios (Extended Data Fig. 6d,e). Thus, IL-27R agonism can synergize with checkpoint blockade therapy to promote control of immunotherapy-resistant tumours.

IL-27 elicits a cytotoxic program in CTLs

To further define the effects of IL-27 on anti-tumour CTLs, we performed scRNA-seq analysis of RPL18-specific CTLs from MC38 tumour-bearing mice treated with IL-27-encoding plasmids, empty control plasmids or IL-27 blockade. Differences between CTLs from tumours and dLNs were a main driver of transcriptional separation regardless of treatment (Extended Data Fig. 7a). To resolve treatment-related effects, we initially performed independent analyses of tumour and dLN-derived cells. Tumour-infiltrating (and, to a lesser extent, dLN-derived) CTLs from IL-27-treated mice were transcriptionally distinct (Fig. 3a,b) and showed increased expression of *Ly6a* and *Gzmb* (Fig. 3c,d), consistent with flow cytometry data (Fig. 2). IL-27 also enhanced expression of the coordinately regulated transcription factors *Stat1*, *Irf1* and *Irf8*[36] (Fig. 3c), which correlated closely with *IL27* in the human melanoma TCGA dataset (*STAT1*, r = 0.65; *IRF1*, r = 0.75; *IRF8*, r = 0.67).

Notably, tumour-infiltrating CTLs (and, to a lesser extent, T cells in dLNs) from IL-27-treated mice showed reduced expression of the exhaustion-promoting transcription factor *Tox*[37,38] (Fig. 3c–f). However, we did not observe differences in other conventional exhaustion markers, including *Pdcd1*, *Lag3*, *Havcr2* or *Tigit* (Extended Data Fig. 7b). Notably, expression of *Tox* and *Gzmb* was largely mutually exclusive (Fig. 3e,f).

To identify transcriptional programs that explain different treatment outcomes, we next performed consensus non-negative matrix factorization (cNMF) on combined tumour- and dLN-derived CTLs, which yielded 17 distinct programs (Fig. 3g,h, Extended Data Figs. 7c and 8 and Supplementary Table 2). Among these, we identified four major IL-27-regulated states: cytotoxicity/STAT1 response (NMF3 and NMF11, including granzymes, *Nkg7*, *Ly6a*, *Ly6c* and *Irf8*), cell cycle activity (NMF4 and NMF12, including *Top2a*, *Ccna2*, *Ccnb1*, *Cdk1* and *Mcm2/3/5/6/7*) and IFN response (NMF7, including *Isg15*, *Mx1*, *Ifit1*, *Ifit3* and *Irf7*) were induced by IL-27, while a program consistent with T precursor exhausted (T_{pex}) cell differentiation (NMF14, including *Tox*, *Slamf6*, *Cd200*, *Gpm6b* and *Cd83*)[39,40] was reduced by IL-27 (Fig. 3g,h and Extended Data Fig. 8). Three programs correlated strongly with
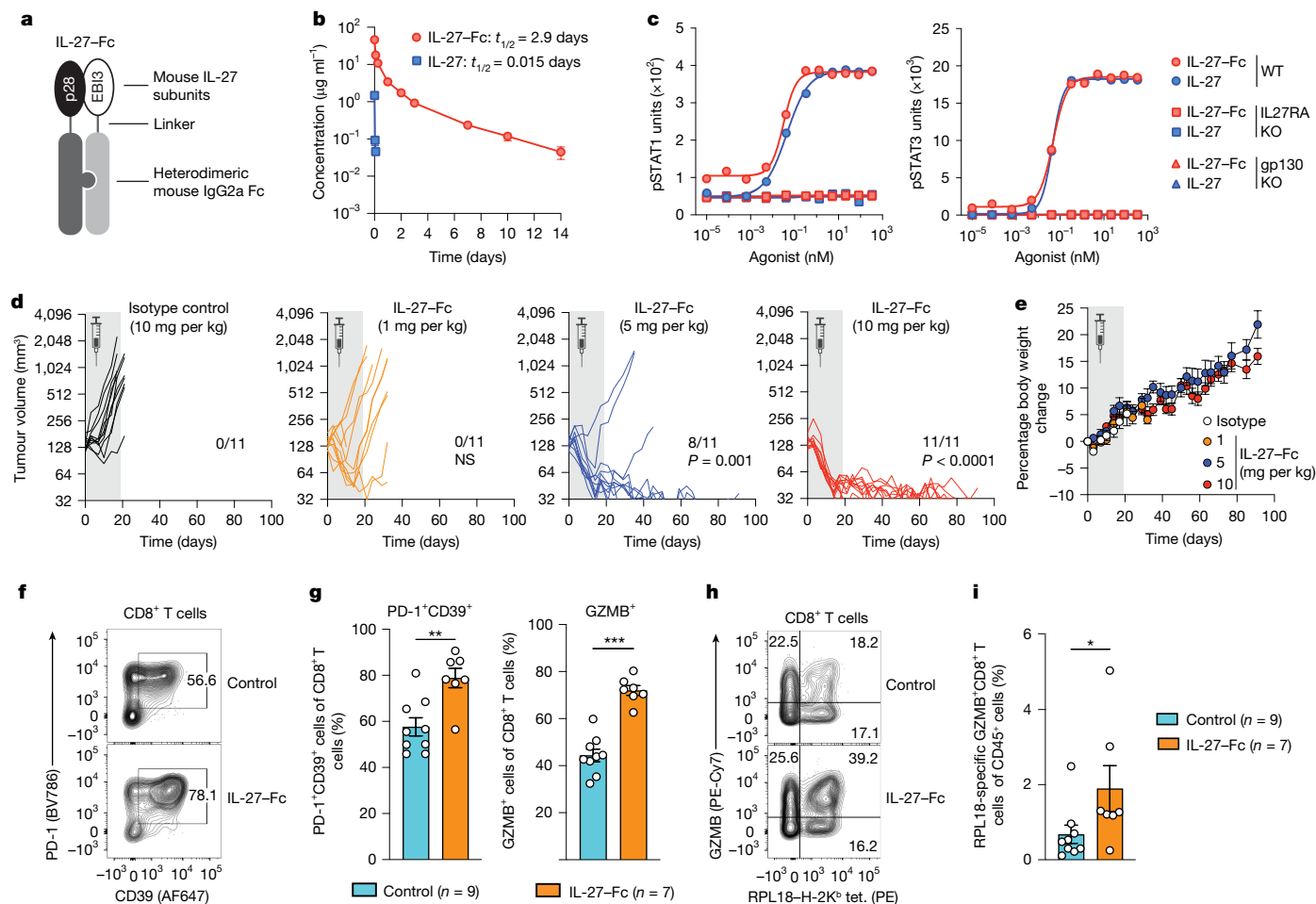
Fig. 3 | IL-27R agonism drives the induction of a cytotoxic phenotype and repression of dysfunctional states in tumour-specific CTLs. a–h, scRNA-seq analysis of RPL18-specific CTLs isolated from MC38 tumours or dLN from mice treated with an IL-27 blocking antibody (anti-IL-27) or IL-27R agonism (IL-27) by HTV injection of an IL-27-encoding plasmid. Control mice were treated with isotype control antibody and injection of an empty vector plasmid. **a**,**b**, UMAP of RPL18-specific CD8^{+} CTLs from tumours (**a**) and dLNs (**b**), coloured according to treatment. **c**,**d**, Pseudobulk differential gene expression between tumour-infiltrating (**c**) and dLN-derived (**d**) CTLs from IL-27 (orange, positive log-transformed fold change (FC)) versus anti-IL-27 (black, negative log-transformed FC) treatment groups. The dashed line represents a *P*-value cut-off of 0.05.

e,**f**, The expression (expr.) of *Tox* and/or *Gzmb* in tumour-infiltrating (**e**) or dLN-derived (**f**) CTLs. Data are shown as log[counts per million (CPM)/100 + 1] units. The dot plot colour and size indicate average expression intensity and the fraction of cells with detectable expression, respectively. **g**,**h**, Three representative cNMF programs (from a total of 17; Extended Data Fig. 8 and Supplementary Table 2) characterized in the tumour (**g**) and dLN (**h**). UMAP plots show the expression intensity (blue, low; yellow, high) across cells. The dot plots indicate the relative contributions of the top five genes for each program. The box plots display the average scores per animal (biological replicates indicated as datapoints, sized according to cell numbers contributed). *P* values were calculated using Wilcoxon rank-sum tests.

CTLsig expression and were induced by IL-27: NMF3 (cytotoxicity/STAT1 response), NMF11 (granzyme[high]) and NMF12 (cell cycle and *Gzmk*) (Extended Data Fig. 7d). By contrast, *Tox* correlated with IL-27-suppressed programs including NMF14 (T$_{pex}$) and NMF15, which included genes associated with CTL dysfunction (such as *Cd244* and *Ikzf2*)[41–44] (Extended Data Fig. 7d). These data suggest that IL-27 induces a proliferative and cytotoxic state in tumour-specific CTLs while limiting their potential for exhaustion.

To evaluate clonal dynamics, we performed single-cell T cell receptor sequencing (TCR-seq) on the same RPL18-specific CTLs. IL-27 did not significantly affect clonal diversity or the fraction of clones shared between matched tumours and dLNs (Extended Data Fig. 7e). The most expanded clones were transcriptionally similar to other expanded cells in the respective treatment group (Extended Data Fig. 7f). Similarly, two clones that were detectable in all of the treatment groups displayed transcriptional patterns consistent with those of their overall respective treatment populations (Extended Data Fig. 7g,h). Notably, when CD8^{+} T cells were engineered to express one of these shared RPL18-specific TCRs and transferred into immunodeficient MC38 tumour-bearing mice, IL-27R agonism enhanced their cytotoxic phenotype (Extended Data Fig. 7i–k). These data suggest that the effects of IL-27R agonism are not restricted to specific tumour-reactive CTL clones.

IL-27 promotes CTL fitness in vitro

We next evaluated the impact of IL-27 on CTLs using an in vitro exhaustion assay. Repetitive stimulation of OT-I cells with OVA$_{257–264}$ peptide[45] induced a dysfunctional phenotype featuring low GZMB production and high expression of TOX. Under these conditions, recombinant IL-27 acted in an IL-27RA-dependent manner to increase SCA-1 and GZMB expression while reducing TOX (Extended Data Fig. 9a–d). As metabolic dysfunction is associated with T cell exhaustion[46], we performed Seahorse metabolic flux analysis and observed that IL-27 enhanced both glycolysis and oxidative phosphorylation under exhaustion-inducing conditions (Extended Data Fig. 9e). Consistent with these effects, OT-I cells killed OVA-expressing tumour cells more efficiently when stimulated with IL-27 (Extended Data Fig. 9f).

We next performed RNA-seq and assay for transposase-accessible chromatin with sequencing (ATAC–seq) to characterize the events downstream of IL-27 signalling. IL-27 promoted transcriptional programs similar to those identified by scRNA-seq in vivo, including JAK–STAT signalling, cytotoxicity and effector memory differentiation, and drove the expression of several transcription factors including *Stat1* and *Irf1*, both of which were induced by IL-27 in tumour-infiltrating CTLs (Extended Data Fig. 9g,h). Notably, IRF1- and STAT1-binding motifs

Fig. 4 | Half-life-extended IL-27 induces tumour regression. a, Schematic of half-life-extended IL-27 (IL-27–Fc). **b,** The pharmacokinetic behaviour of recombinant mouse IL-27 versus IL-27–Fc in C57BL/6J mice. **c,** Mouse BW5147.3 T lymphoblasts were modified using CRISPR–Cas9 to delete IL-27RA or gp130. Cells were treated with varying doses of recombinant IL-27 or IL-27–Fc and phosphorylated STAT1 (Tyr701) and STAT3 (Tyr705) were quantified in the cell lysates after 30 min. **d**–**i,** C57BL/6J mice were engrafted with MC38 cells. When tumours reached 150 mm³ (day 0), the mice were treated every 3 days with a control antibody or IL-27–Fc. **d,** The tumour volumes and durable response frequencies. Statistical analysis was performed using Fisher's exact tests

versus the control group. Mice received a total of six doses (the dosing window is indicated by the grey shading). **e,** Mouse body weights (mean ± s.e.m.) associated with data from **d.** The syringe icons in **d** and **e** were created using BioRender. **f**–**i,** Seven days after treatment, tumours were collected for flow cytometry analysis. **f,** Representative staining of PD-1 and CD39. **g,** The frequencies of PD-1⁺CD39⁺ and GZMB⁺ cells in CTLs. **h,** Representative staining of RPL18-H-2Kᵇ tetramer and GZMB. **i,** The frequencies of RPL18-specific GZMB⁺ CTLs among tumour-infiltrating CD45⁺ cells. For **g** and **i,** data are mean ± s.e.m. Statistical analysis was performed using two-sided Mann–Whitney *U*-tests (**g** and **i**). For **f**–**i,** data are representative of three experiments.

were strongly enriched in open chromatin regions of IL-27-treated CTLs (Extended Data Fig. 9i), implying their direct involvement in IL-27-induced programs, consistent with human virus-specific T cells[47]. Indeed, we observed strong concordance between IL-27-induced *Irf1* or *Stat1* expression and corresponding transcription factor activity inferred from differentially accessible promoter sites containing IRF1 or STAT1 motifs (Extended Data Fig. 9j).

IL-27–Fc induces tumour regression

To improve the pharmacological properties of IL-27, we designed a heterodimeric protein in which EBI3 and IL-27p28 are fused to mouse IgG2a Fc sequences (IL-27–Fc; Fig. 4a). Whereas recombinant IL-27 was cleared rapidly in mice ($t_{1/2} < 30$ min), the serum half-life of IL-27–Fc was increased nearly 200-fold ($t_{1/2} = 2.9$ days; Fig. 4b), and IL-27–Fc activated STAT1 and STAT3 with a potency equal to WT IL-27 (Fig. 4c). IL-27–Fc was well tolerated and induced dose-dependent tumour regression (Fig. 4d,e). Like overexpressed IL-27, IL-27–Fc increased the frequency of activated CD39⁺PD-1⁺ and GZMB⁺ CTLs, the CTL/T_reg cell ratio and the abundance of GZMB⁺ RPL18-specific CTLs (Fig. 4f–i and Extended Data

Fig. 9k). Notably, IL-27–Fc treatment did not control tumour growth or enhance CTL function in mice with CTL-restricted IL-27RA deficiency (Extended Data Fig. 9l–o).

IL-27 expression predicts CIT efficacy

To determine whether IL-27 is associated with CIT efficacy in humans, we evaluated pre-treatment tumour RNA-seq data from randomized clinical trials of atezolizumab (anti-PD-L1) versus chemotherapy in patients with metastatic urothelial bladder carcinoma (mUC; IMvigor210 and IMvigor211) or non-small cell lung carcinoma (mNSCLC; OAK). To identify IL-27^high patients, we selected those with high (≥upper quartile) expression of both *IL27* and *EBI3*. IL-27^high tumours were also high for CTLsig expression and genes associated with macrophages and DCs (Extended Data Fig. 10a). Gene Ontology analysis confirmed that IL-27^high status was associated with various adaptive immunological processes (Extended Data Fig. 10b). Similarly, IL-27^high status was associated with an inflamed histological phenotype (Extended Data Fig. 10c). Notably, atezolizumab treatment was associated with increased overall survival (OS) compared with chemotherapy in IL-27^high patients (IMvigor210/211,
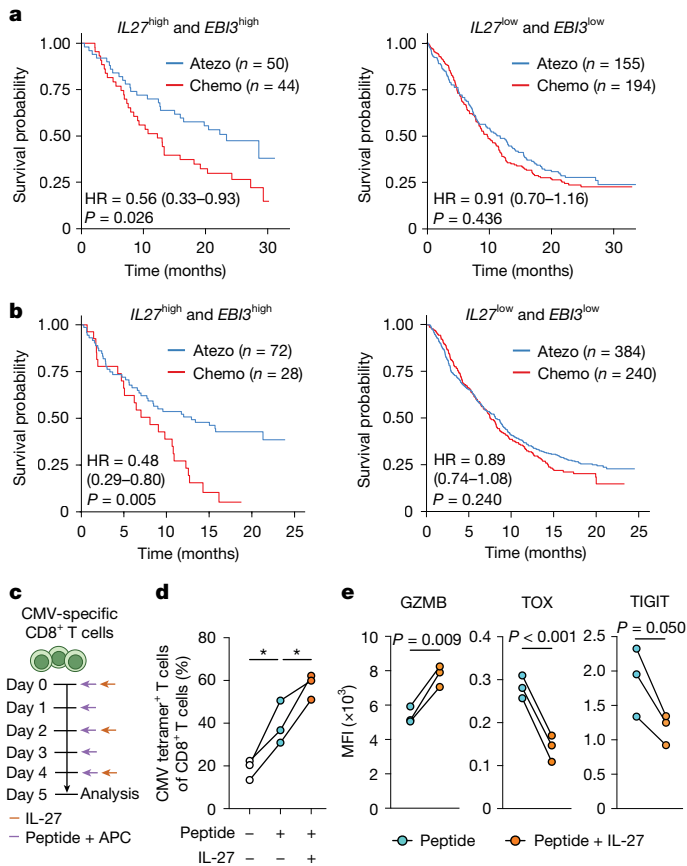
Fig. 5 | IL-27 predicts immunotherapy response in patients with cancer and promotes human CTL function. a,b, OS in patients with mNSCLC from the OAK phase 3 study (**a**) or mUC from a combined dataset of the IMvigor211 phase 3 and IMvigor210 (cohort 2) phase 2 studies (**b**). Patients were treated with the PD-L1 blocking antibody atezolizumab (atezo) or chemotherapy (chemo) and categorized based on high (≥upper quartile) or low (<upper quartile) mRNA expression of *IL27* and *EBI3* in pre-treatment tumour biopsies. *P* values and hazard ratios (with the 95% confidence intervals (CIs)) were calculated using the log-rank test and a Cox regression model. See also Extended Data Fig. 10. **c**–**e**, The effects of IL-27 on repetitively stimulated CMV-specific human CTLs. **c**, The experimental approach. Bulk primary human CTLs (from three healthy donors) were engineered to express a CMV-pp65-specific TCR (resulting in a mixture of CMV-specific and non-specific cells) and stimulated daily with peptide-loaded APCs with or without IL-27 (25 ng ml^{-1}). **d**, The frequency of CMV-specific cells among total T cells, determined by MHC-I tetramer staining. **e**, GZMB, TOX and TIGIT expression in CMV-specific cells. Groups were compared using two-sided *t*-tests. Data are representative of two independent experiments, each with *n* = 3 independent donors. MFI, mean fluorescence intensity.

hazard ratio (HR) = 0.48, *P* = 0.005; OAK, HR = 0.56, *P* = 0.026), but not in patients with low expression of *IL27* and/or *EBI3* (Fig. 5a,b and Extended Data Fig. 10d,e). Likewise, IL-27^{high} status correlated with improved OS in patients who were treated with atezolizumab, but not chemotherapy (Extended Data Fig. 10f,g). Thus, high expression of IL-27 may predict increased clinical efficacy of anti-PD-L1 therapy.

We next investigated *IL27* expression dynamics using published RNA-seq data from pre-treatment and on-treatment melanoma biopsies from patients treated with nivolumab (anti-PD-1)[48]. Although pre-treatment expression of *IL27* and *EBI3* did not associate significantly with clinical response in this dataset, *IL27* expression was elevated significantly during treatment in responsive patients, but not in non-responsive patients. Consequently, high on-treatment *IL27* expression was associated specifically with responsive tumours (Extended Data Fig. 10h,i). Similar changes were observed for *EBI3*, but not other IL-27-related cytokines, including *IL12A*, *IL12B* and *IL23A*

(Extended Data Fig. 10i). Indeed, among all cytokines with detectable expression, only *IL27*, *IL32* and *TNFSF13* (encoding APRIL) displayed significant on-treatment induction in responsive patients (Extended Data Fig. 10h). Consistent with these findings, increased on-treatment *IL27* was associated with higher response frequency and prolonged patient survival (HR = 0.38, *P* = 0.0162; Extended Data Fig. 10j,k). Larger studies will be required to determine conclusively whether this association is independent of the relationship between IL-27 and T cell infiltration.

IL-27 promotes human CTL function

To evaluate the effect of IL-27 on human CTLs, we adapted the mouse exhaustion assay (Extended Data Fig. 9) by engineering primary human CD8$^+$ T cells to express a cytomegalovirus (CMV)-specific TCR[49]. When these cells were stimulated repetitively using antigen-presenting cells pulsed with CMV-pp65 peptide (Fig. 5c), IL-27 promoted the expansion of CMV-specific T cells (Fig. 5d) and expression of GZMB, while it suppressed dysfunction-associated markers including TOX and TIGIT[37,50] (Fig. 5e and Extended Data Fig. 10l). RNA-seq analysis demonstrated that IL-27 promoted cytotoxic and effector memory differentiation (Extended Data Fig. 10m), consistent with mouse CTLs and the recent discovery that IL-27 signalling is required for normal human CTL responses to Epstein–Barr virus[51].

Discussion

Our data suggest that IL-27 has an important supportive role for tumour-specific CTLs. While impaired IL-27 signalling attenuates the persistence and cytotoxicity of anti-tumour CTLs, these properties are enhanced by IL-27R agonism. These findings are supported by the association between IL-27 expression and immunotherapy efficacy in the clinic. Previous studies have suggested that IL-27 induces T cell dysfunction by promoting expression of immunoregulatory factors including PD-1 and CD39[11,12,52]. However, our data suggest that expression of these markers by IL-27-stimulated cells is probably attributable to efficient activation, consistent with previous studies linking increased IL-27 expression with improved tumour control[8,9] and with observations that highly functional effector cells express co-inhibitory receptors such as PD-1[53–55].

Tumour-specific CTLs are thought to become exhausted through multiple transitory states, including the progenitor-like T$_{pex}$ phenotype. This process is orchestrated by several key transcription factors, including TOX[37,38,56]. In our studies, IL-27 suppressed both *Tox* expression and a T$_{pex}$-like phenotype in CTLs in vivo. Notably, a recent study identified an exhaustion-resistant CTL phenotype characterized by high expression of STAT-response genes, similar to IL-27-stimulated cells in our experiments[57]. Although further studies are needed to clarify the mechanism by which IL-27 decouples cytotoxic programming from the T$_{pex}$-to-exhausted fate, our data suggest the involvement of STAT1, STAT3 and IRF1. Others have reported that CTL responses to vaccines require IL-27-induced STAT1 and STAT3 activity[58]. Similarly, STAT1, IRF1 and STAT3 are known to promote survival and effector function of virus- or tumour-specific CTLs[59,60]. Despite these remaining questions, our data demonstrate that IL-27 sustains fitness and cytotoxic function of tumour-specific CTLs, revealing its potential as an immunomodulatory target in cancer.

Online content

Any methods, additional references, Nature Portfolio reporting summaries, source data, extended data, supplementary information, acknowledgements, peer review information; details of author contributions and competing interests; and statements of data and code availability are available at https://doi.org/10.1038/s41586-024-08510-w.

Article

1. Philip, M. & Schietinger, A. CD8⁺ T cell differentiation and dysfunction in cancer. *Nat. Rev. Immunol.* **22**, 209–223 (2022).
2. Propper, D. J. & Balkwill, F. R. Harnessing cytokines and chemokines for cancer therapy. *Nat. Rev. Clin. Oncol.* **19**, 237–253 (2022).
3. Holder, P. G. et al. Engineering interferons and interleukins for cancer immunotherapy. *Adv. Drug Deliv. Rev.* **182**, 114112 (2022).
4. Yoshida, H. & Hunter, C. A. The immunobiology of interleukin-27. *Annu. Rev. Immunol.* **33**, 417–443 (2015).
5. Fabbi, M., Carbotti, G. & Ferrini, S. Dual roles of IL-27 in cancer biology and immunotherapy. *Mediat. Inflamm.* **2017**, 3958069 (2017).
6. Pagano, G. et al. Interleukin-27 potentiates CD8+ T-cell-mediated antitumor immunity in chronic lymphocytic leukemia. *Haematologica* **108**, 3011–3024 (2023).
7. Liu, Z. et al. Epstein-Barr virus-induced gene 3-deficiency leads to impaired antitumor T-cell responses and accelerated tumor growth. *OncoImmunology* **4**, e989137 (2015).
8. Liu, Z. et al. IL-27 enhances the survival of tumor antigen-specific CD8⁺ T cells and programs them into IL-10-producing, memory precursor-like effector cells. *Eur. J. Immunol.* **43**, 468–479 (2013).
9. Zhu, J. et al. IL-27 gene therapy induces depletion of Tregs and enhances the efficacy of cancer immunotherapy. *JCI Insight* **3**, e98745 (2018).
10. Ding, M. et al. IL-27 improves adoptive CD8⁺ T cells' antitumor activity via enhancing cell survival and memory T cell differentiation. *Cancer Sci.* **113**, 2258–2271 (2022).
11. Chihara, N. Induction and transcriptional regulation of the co-inhibitory gene module in T cells. *Nature* **558**, 454–459 (2018).
12. DeLong, J. H. et al. IL-27 and TCR stimulation promote T cell expression of multiple inhibitory receptors. *ImmunoHorizons* **3**, 13–25 (2019).
13. Clemente, C. G. et al. Prognostic value of tumor infiltrating lymphocytes in the vertical growth phase of primary cutaneous melanoma. *Cancer* **77**, 1303–1310 (1996).
14. Huang, A. C. & Zappasodi, R. A decade of checkpoint blockade immunotherapy in melanoma: understanding the molecular basis for immune sensitivity and resistance. *Nat. Immunol.* **23**, 660–670 (2022).
15. Georgiev, P. et al. Reverse translating molecular determinants of anti-programmed death 1 immunotherapy response in mouse syngeneic tumor models. *Mol. Cancer Ther.* **21**, 427–439 (2022).
16. Pflanz, S. et al. IL-27, a heterodimeric cytokine composed of EBI3 and p28 protein, induces proliferation of naive CD4⁺ T cells. *Immunity* **16**, 779–790 (2002).
17. McDermott, D. F. et al. Clinical activity and molecular correlates of response to atezolizumab alone or in combination with bevacizumab versus sunitinib in renal cell carcinoma. *Nat. Med.* **24**, 749–757 (2018).
18. Awasthi, A. et al. A dominant function for interleukin 27 in generating interleukin 10-producing anti-inflammatory T cells. *Nat. Immunol.* **8**, 1380–1389 (2007).
19. Batten, M. et al. IL-27 supports germinal center function by enhancing IL-21 production and the function of T follicular helper cells. *J. Exp. Med.* **207**, 2895–2906 (2010).
20. Yadav, M. et al. Predicting immunogenic tumour mutations by combining mass spectrometry and exome sequencing. *Nature* **515**, 572–576 (2014).
21. Ngiow, S. F. et al. A threshold level of intratumor CD8⁺ T-cell PD1 expression dictates therapeutic response to anti-PD1. *Cancer Res.* **75**, 3800–3811 (2015).
22. Juneja, V. R. et al. PD-L1 on tumor cells is sufficient for immune evasion in immunogenic tumors and inhibits CD8 T cell cytotoxicity. *J. Exp. Med.* **214**, 895–904 (2017).
23. Pflanz, S. et al. WSX-1 and glycoprotein 130 constitute a signal-transducing receptor for IL-27. *J. Immunol.* **172**, 2225–2231 (2004).
24. Hirahara, K. et al. Asymmetric action of STAT transcription factors drives transcriptional outputs and cytokine specificity. *Immunity* **42**, 877–889 (2015).
25. Duhen, T. et al. Co-expression of CD39 and CD103 identifies tumor-reactive CD8 T cells in human solid tumors. *Nat. Commun.* **9**, 2724 (2018).
26. DeLong, J. H. et al. Cytokine- and TCR-mediated regulation of T cell expression of Ly6C and Sca-1. *J. Immunol.* **200**, 1761–1770 (2018).
27. Bailey, C. M. et al. Targeting HIF-1α abrogates PD-L1-mediated immune evasion in tumor microenvironment but promotes tolerance in normal tissues. *J. Clin. Investig.* **132**, e150846 (2022).
28. Hos, B. J. et al. Identification of a neo-epitope dominating endogenous CD8 T cell responses to MC-38 colorectal cancer. *OncoImmunology* **9**, 1673125 (2020).
29. Xu, W.-D., Wang, D.-C., Zhao, M. & Huang, A.-F. An updated advancement of bifunctional IL-27 in inflammatory autoimmune diseases. *Front. Immunol.* **15**, 1366377 (2024).
30. Maekawa, Y. et al. Notch2 integrates signaling by the transcription factors RBP-J and CREB1 to promote T cell cytotoxicity. *Nat. Immunol.* **9**, 1140–1147 (2008).
31. Müller, S. I. et al. A folding switch regulates interleukin 27 biogenesis and secretion of its α-subunit as a cytokine. *Proc. Natl Acad. Sci. USA* **116**, 1585–1590 (2019).
32. Zhang, G., Budker, V. & Wolff, J. A. High levels of foreign gene expression in hepatocytes after tail vein injections of naked plasmid DNA. *Hum. Gene Ther.* **10**, 1735–1737 (1999).
33. Liu, F., Song, Y. K. & Liu, D. Hydrodynamics-based transfection in animals by systemic administration of plasmid DNA. *Gene Ther.* **6**, 1258–1266 (1999).
34. Hirahara, K. et al. Interleukin-27 priming of T cells controls IL-17 production in trans via induction of the ligand PD-L1. *Immunity* **36**, 1017–1030 (2012).
35. Kleffel, S. et al. Melanoma cell-intrinsic PD-1 receptor functions promote tumor growth. *Cell* **162**, 1242–1256 (2015).
36. Langlais, D., Barreiro, L. B. & Gros, P. The macrophage IRF8/IRF1 regulome is required for protection against infections and is associated with chronic inflammation. *J. Exp. Med.* **213**, 585–603 (2016).
37. Khan, O. et al. TOX transcriptionally and epigenetically programs CD8⁺ T cell exhaustion. *Nature* **571**, 211–218 (2019).
38. Scott, A. C. et al. TOX is a critical regulator of tumour-specific T cell differentiation. *Nature* **571**, 270–274 (2019).
39. Castiglioni, A. et al. Combined PD-L1/TGFβ blockade allows expansion and differentiation of stem cell-like CD8 T cells in immune excluded tumors. *Nat. Commun.* **14**, 4703 (2023).
40. Andreatta, M. et al. Interpretation of T cell states from single-cell transcriptomics data using reference atlases. *Nat. Commun.* **12**, 2965 (2021).
41. Das, K. M. P. et al. Hypoxia-inducible lipid droplet-associated protein inhibits adipose triglyceride lipase. *J. Lipid Res.* **59**, 531–541 (2018).
42. McIntyre, A. & Harris, A. L. Metabolic and hypoxic adaptation to anti-angiogenic therapy: a target for induced essentiality. *EMBO Mol. Med.* **7**, 368–379 (2015).
43. Agresta, L., Hoebe, K. H. N. & Janssen, E. M. The emerging role of CD244 signaling in immune cells of the tumor microenvironment. *Front. Immunol.* **9**, 2809 (2018).
44. McLane, L. M., Abdel-Hakeem, M. S. & Wherry, E. J. CD8 T cell exhaustion during chronic viral infection and cancer. *Annu. Rev. Immunol.* **37**, 457–495 (2019).
45. Zhao, M. et al. Rapid in vitro generation of bona fide exhausted CD8⁺ T cells is accompanied by Tcf7 promotor methylation. *PLoS Pathog.* **16**, e1008555 (2020).
46. Vardhana, S. A. et al. Impaired mitochondrial oxidative phosphorylation limits the self-renewal of T cells exposed to persistent antigen. *Nat. Immunol.* **21**, 1022–1033 (2020).
47. Cheng, J. et al. IL-27 induces IFN/STAT1-dependent genes and enhances function of TIGIT⁺ HIVGag-specific T cells. *iScience* **25**, 103588 (2022).
48. Riaz, N. et al. Tumor and microenvironment evolution during immunotherapy with nivolumab. *Cell* **171**, 934–949 (2017).
49. Schober, K. et al. Orthotopic replacement of T-cell receptor α- and β-chains with preservation of near-physiological T-cell function. *Nat. Biomed. Eng.* **3**, 974–984 (2019).
50. Johnston, R. J. et al. The immunoreceptor TIGIT regulates antitumor and antiviral CD8⁺ T cell effector function. *Cancer Cell* **26**, 923–937 (2014).
51. Martin, E. et al. Role of IL-27 in Epstein–Barr virus infection revealed by IL-27RA deficiency. *Nature* **628**, 620–629 (2024).
52. Zhu, C. et al. An IL-27/NFIL3 signalling axis drives Tim-3 and IL-10 expression and T-cell dysfunction. *Nat. Commun.* **6**, 6072 (2015).
53. Ahn, E. et al. Role of PD-1 during effector CD8 T cell differentiation. *Proc. Natl Acad. Sci. USA* **115**, 4749–4754 (2018).
54. Xiong, H. et al. Coexpression of inhibitory receptors enriches for activated and functional CD8⁺ T cells in murine syngeneic tumor models. *Cancer Immunol. Res.* **7**, 963–976 (2019).
55. Gerhardt, L., Hong, M. M. Y., Yousefi, Y., Figueredo, R. & Vareki, S. M. IL-12 and IL-27 promote CD39 expression on CD8⁺ T cells and differentially regulate the CD39⁺CD8⁺ T cell phenotype. *J. Immunol.* **210**, 1598–1606 (2023).
56. Blank, C. U. et al. Defining 'T cell exhaustion'. *Nat. Rev. Immunol.* **19**, 665–674 (2019).
57. Rudloff, M. W. et al. Hallmarks of CD8⁺ T cell dysfunction are established within hours of tumor antigen encounter before cell division. *Nat. Immunol.* **24**, 1527–1539 (2023).
58. Pennock, N. D., Gapin, L. & Kedl, R. M. IL-27 is required for shaping the magnitude, affinity distribution, and memory of T cells responding to subunit immunization. *Proc. Natl Acad. Sci. USA* **111**, 16472–16477 (2014).
59. Huang, Z. et al. IL-27 promotes the expansion of self-renewing CD8+ T cells in persistent viral infection. *J. Exp. Med.* **216**, 1791–1808 (2019).
60. Miyagawa, F. et al. Interferon regulatory factor 8 integrates T-cell receptor and cytokine-signaling pathways and drives effector differentiation of CD8 T cells. *Proc. Natl Acad. Sci. USA* **109**, 12123–12128 (2012).

Methods

Mice

CD45.2+ C57BL/6J (JAX, 000664), CD45.1+ C57BL/6J (JAX, 002014), *Ebi3*[−/−61] (JAX, 008691), and *Foxp3-GFP*[62,63] (JAX, 006772) mice were purchased from Jackson Laboratories. *Rag2*^{−/−} mice were purchased from Taconic (RAGN12) or Jackson Laboratories (JAX, 008449). C57BL/6J OT-I TCR-transgenic mice[64] (JAX, 003831) were purchased from the Jackson Laboratory and bred at Genentech. *Il27ra*^{−/−} mice (and *Il27ra*^{+/+} littermate controls) were generated and bred at Genentech[65].

The *Il27ra* conditional KO (CKO) allele was generated using C57BL/6N C2 ES cells and established methods to obtain chimeras and germline transmission of the allele. A targeting vector consisting of a 5′ homology arm, a loxP site, the exon 2 region to be floxed, an FRT-Neo-FRT-loxP cassette and a 3′ homology arm was used to create the CKO allele in ES cells. The Neo selection cassette was excised by FlpO treatment, leaving a residual FRT site. The CKO allele was verified by sequencing before ES cell microinjection. The resulting heterozygous N1 mice were bred with C57BL/6N to establish a breeding colony. The 493 bp floxed *Il27ra* region corresponds to GRCm39/mm39 chromosome 8:84768452–84768944. *Il27ra*-floxed mice were crossed with *E8i.Cd8a-Cre* mice[30] (JAX, 008766) to delete *Il27ra* expression specifically in peripheral CD8+ T cells.

The *Il27* CKO allele was generated using established CRISPR methodology and electroporation of Cas9 HiFi (IDT) in complex with two sgRNAs, along with a single-stranded donor template into C57BL/6N zygotes: 5′ sgRNA located upstream of *Il27* exon 2 (5′-CACUGUUGUAA-GAACACCAA-3′); and 3′ sgRNA located downstream of *Il27* exon 3 (5′-GAUGGGCUGACGACUGUGAU-3′). The resulting mosaic founders were screened for predicted off-target effects, backcrossed to C57BL/6N and off-target-free N1 heterozygous mice with the desired mutation(s) were bred with C57BL/6N mice to establish a breeding colony. The CKO allele was verified by sequencing. The 823 bp floxed *Il27* region corresponds to GRCm39/mm39 chromosome 7:126191446–126192268 (reverse strand). *Il27*-floxed mice were bred with *LysM-cre*[66] or *Clec9a-cre*[67] mice to abolish IL-27 production in phagocytic myeloid cells and DCs, respectively.

Female and male mice aged 6 to 16 weeks were used for experiments. All mice were housed at Genentech in individually ventilated cages within animal rooms maintained under a 14 h–10 h light–dark cycle. Animal rooms were temperature and humidity controlled, between 20 °C and 26 °C and 30% and 70% humidity, respectively, with 10 to 15 room air exchanges per hour. Mice were acclimatized to the study conditions for at least 3 days before tumour cell implantation. All of the animal studies were approved by Genentech's Institutional Animal Care and Use Committee and adhere to the NRC Guidelines for the Care and Use of Laboratory Animals.

Antibodies for in vivo studies

Anti-mouse PD-L1 (6E11, mIgG2a), anti-mouse IL-27 (4066v10S, mIgG2a) and isotype control monoclonal antibodies were developed and produced in-house at Genentech using standard hybridoma technology. Generated by immunizing hamsters, anti-mouse IL-27 (4066v10S) CDRs were grafted into the closest mouse framework along with a few key framework positions to produce a fully mouse antibody. The ability of anti-IL-27 (4066v10S) to neutralize IL-27 function in vivo was confirmed using a model of recombinant IL-27 challenge. In brief, 24 h before intravenous administration of 10 μg of recombinant mouse IL-27 (R&D Systems, 2799-ML), mice were treated with varying doses of IL-27 blocking antibody. Then, 20 min after IL-27 challenge, the spleens were collected and lysed for detection of phosphorylated STAT1 (Tyr701) using the HTRF assay kit (Cisbio, 63ADK026PEG) and phosphorylated STAT3 (Tyr705) using an electrochemiluminescence-based immunoassay (MSD, K150SVD).

In vivo tumour studies

The MC38 cell line was obtained from the University of Leiden. The E0771 cell line was purchased from CH3 Biosystems. The B16-F10 cell line was obtained from American Type Culture Collection (ATCC). All of the cell lines were stored by a common cell repository at Genentech. Cell lines are routinely screened, and all cells used in this study were negative for mycoplasma and authenticated by RNA-seq analysis. Two methods of mycoplasma detection were used to avoid false positive/negative results: Lonza Mycoalert and Stratagene Mycosensor. Cells were cultured in RPMI 1640 medium plus 2 mM L-glutamine with 10% fetal bovine serum (FBS; Hyclone). Cells in log-phase growth were centrifuged, washed with Hank's balanced salt solution (HBSS), counted and resuspended in 50% HBSS and 50% Matrigel (BD Biosciences). Female C57BL/6J mice (aged 6–10 weeks) were obtained from Charles River Laboratories, housed at Genentech in standard rodent micro-isolator cages and acclimatized for at least 3 days before cell injection. E0771 cells were inoculated in the left #5 mammary fat pad (1×10^5 cells in 100 μl of HBSS/Matrigel mixture). Mice were inoculated subcutaneously in the right flank with 1×10^5 B16-F10 cells or 1×10^6 MC38 cells. When tumours reached a volume of 100–200 mm³ (approximately 8–12 days after inoculation), the mice were distributed into treatment groups such that variance in tumour sizes between treatment groups was minimized.

Mice were treated with isotype control antibodies, anti-PD-L1 (mouse IgG1, 6E11, 10 mg per kg first dose followed by 5 mg per kg thereafter, twice a week), anti-IL-27 (mouse IgG2a, 25 mg per kg twice a week) or a single HTV injection of control or IL-27 encoding plasmid. Anti-PDL1, anti-IL-27 and isotype control antibodies were produced in-house and were free of endotoxin contamination.

For pharmacodynamic/phenotyping studies, mice were euthanized after 7 days (after three doses of antibody treatment or one HTV treatment) and lymph nodes and tumours were collected for flow cytometry analysis. For therapeutic efficacy studies, HTV was done once, and antibodies were administered twice per week for 3 weeks (intravenously for the first dose and intraperitoneally thereafter). Tumours were measured twice per week using digital callipers, and the tumour volumes were calculated using the modified ellipsoid formula, $1/2 \times (\text{length} \times \text{width}^2)$. When the tumour volumes fell below 32 mm³ they were considered a CR. Tumours that regressed but eventually recurred were considered partial responders, and tumours that never regressed were considered to be progressive disease. Disease progression was defined as a 5× increase in tumour volume. Mice were euthanized if tumours ulcerated or volumes exceeded 1,500–2,000 mm³. Early euthanasia of some mice due to tumour ulceration contributed to some variability in final sample sizes of immune pharmacodynamic studies. No mice met criteria for euthanasia due to body weight loss or adverse clinical signs. Sample sizes in the mouse studies were based on the number of mice routinely needed to establish statistical significance based on variability within study arms. Investigators were not blinded to treatment.

For bone marrow chimera experiments, C57BL/6J CD45.1 recipients were sublethally irradiated with one 4.5 Gray dose of gamma irradiation from a caesium source and received 6×10^6 bone marrow cells from either *Il27ra*^{−/−} mice or *Il27ra*^{+/+} littermate controls by intravenous injection. Chimeric mice were analysed at least 4 weeks after transplantation to allow sufficient time for haematopoietic reconstitution.

Plasmid generation and HTV injection

Constructs encoding a linked version of IL-27-Ebi3 (EBI3.M1-P228.4x(GGGS).IL-27A.F29-S234) were cloned into the mammalian pCAGG expression plasmid (Addgene) and used for HTV injection. The HTV technique involves rapid injection (5–7 s) of a large volume (8–12% body weight) of solution containing 50 μg of plasmid into the tail vein of mice.

Article

Tissue preparation and flow cytometry

Tumours were collected, weighed and digested using tumour dissociation kit solution (Miltenyi, 130-096-730) in GentleMACS (Miltenyi) tubes using the programs mouse TDK1 for MC38 and B16-F10 and TDK2 for E0771. Lymph nodes were enzymatically digested using a cocktail of dispase (0.8 mg ml^{-1}; Life Technologies), collagenase P (0.2 mg ml^{-1}) and DNase I (0.1 mg ml^{-1}; Roche) for 20 min at 37 °C to obtain a single-cell suspension. Cells were counted using the Vi-CELL XR (Beckman Coulter) system. For cytokine staining, cell suspensions were stimulated with eBioscience Cell Stimulation Cocktail plus protein transport inhibitors (00-4975-93) in RPMI medium with 10% FBS plus 2 mM L-glutamine and 2-mercaptoethanol for 2.5 h at 37 °C. The samples were then passed through a 70 μm filter and prepared for flow cytometry. Cells were labelled with monoclonal antibodies at 4 °C for 20–30 min. Before cell surface staining with fluorescently labelled antibodies, cells were labelled with live/dead fixable viability efluor780 stain in PBS (Thermo Fisher Scientific) to exclude dead cells from downstream analyses, then preincubated with Fc receptor blocking antibody (2.4G2, 1:100, 553142, BD Biosciences). For intracellular staining, cells were first stained for surface antigens, then fixed with FOXP3 fixation buffer (005523, eBioscience) for 40 min in the dark at room temperature and then washed twice with permeabilization/wash buffer (008333, eBioscience) and stained with a mix of intracellular antibodies for 30 min at 4 °C in the dark. Appropriate isotype controls were included for staining of transcription factors. Cells were collected on the Symphony flow cytometer (BD Biosciences) and analysed using FlowJo software (v.10.8.1, Treestar). Flow cytometry labelling (without inclusion of Feature Barcoding antibodies from BioLegend) was performed in PBS supplemented with 0.5% FBS. Anti-mouse IL-27RA (9527, mIgG2a) was generated at Genentech. Detailed information on the flow cytometry antibodies used in this study is provided in Supplementary Table 3, and a general gating strategy for identification and analysis of T cells from mouse tissues is provided in Supplementary Fig. 1.

IL-27–Fc cloning, protein expression and purification

The heterodimeric monovalent IL-27–Fc knob-into-hole fusion protein was produced as follows. A protein expression construct was prepared that contains the cDNA sequence for mouse EBI3 amino acids 1–228 (UniProt: O35228) fused to mouse IgG2a containing LALAPG mutations (L234A/L235A/P329G) and an additional Fc hole mutation (L368A, Y407V). Similarly, another protein construct was generated that contains the cDNA sequence for mouse p28 amino acids 1–234 (UniProt: Q8K3I6) fused to the same mouse IgG2a with LALAPG mutations, but with an Fc knob mutation (T366W). The cDNAs for the two protein constructs were synthesized (GenScript) and subsequently subcloned into the pRK vector driven by a CMV promoter (Genentech). Protein expression was initiated by transiently co-transfecting the EBI3 and p28 vectors in Chinese hamster ovary (CHO) cells. The supernatant containing IL-27–Fc was purified by standard preparative protein A chromatography followed by gel filtration. Ion-exchange chromatography was further performed to remove impurities and IL-27–Fc was dialysed in 20 mM histidine acetate and 150 mM NaCl at pH 5.5. Purity and aggregation of IL-27–Fc were determined by SDS–PAGE under non-reducing and reducing conditions. Protein aggregation was assessed using SEC–MALS size-exclusion chromatography (Waters, XBirdge Protein BEH SEC column) with multi-angle light scattering (Wyatt).

Pharmacokinetic analysis of mouse IL-27–Fc

Three groups of female C57BL/6 mice ($n = 4$ per group), aged 6–8 weeks, were serially sampled. Mice received a single intravenous dose of 3 mg per kg IL-27–Fc or 1 mg per kg WT recombinant IL-27. The serum samples were collected at 0.1667, 2, 6, 24, 48, 72, 168, 240 and 336 h post-dose for the IL-27–Fc group and 0.1667, 1, 2, 4, 6, 24 and 48 h post-dose for the IL-27 group. The IL-27 concentrations in the serum were quantified using the mouse IL-27 ELISA developed by Genentech (Genentech). This assay uses rat anti-mouse IL-27 for capture and biotinylated rat anti-mouse IL-27 for detection. The minimum dilution required for this assay was 1:20. The assay offers standard curve ranges of 0.01562–2 μg ml^{-1} for mouse WT IL-27 and 0.00196–0.25 μg ml^{-1} for IL-27–Fc in mouse serum.

In vitro cytotoxicity assay

MC38-mKate or MC38-OVA-GFP cells were maintained in RPMI 1640 supplemented with 10% FBS (Gibco), 100 U ml^{-1} penicillin–streptomycin (Life Technologies) and 2 mM L-glutamine (Life Technologies), and were cultured at 37 °C in 5% CO$_2$. MC38 cells were treated overnight with 20 ng ml^{-1} of IFNγ, washed and then put in culture with T$_{eff}$ cells (effector:target ratios, 10:1). Images were taken every hour over a 3 day period using the Incucyte Zoom system.

scRNA-seq and TCR-seq sample processing and sequencing

For RPL18-specific CD8$^+$ T cell sorting (for TCR/scRNA-seq), cells from tumour and lymph node digests were enriched for CD8$^+$ T cells by negative selection using the EasySep mouse CD8$^+$ T cell Isolation Kit (StemCell Technologies, 19853). Enriched lymphocytes were subsequently stained and sorted using fluorescence-activated cell sorting (FACS) for scRNA-seq. Cells were labelled with PE-conjugated and barcoded (total-seq C0952, BioLegend) RPL18-H-2K^b tetramer for 20 min at room temperature, then stained for surface antigens (CD8, CD45.2, Thy1.2, CD4) plus one of the following Hashtag antibodies (one for each replicate, 5 μg ml^{-1}): TotalSeq C0301 (barcode sequence: ACCCACCAGTAAGAC), C0302 (barcode sequence: GGTCGAGAGCATTCA), C0303 (barcode sequence: CTTGCCGCATGTCAT), C0304 (barcode sequence: AAAGCATTCTTCACG) C0305 (barcode sequence: CTTTGTCTTTGTGAG), C0306 (barcode sequence: TATGCTGCCACGGTA), C0307 (barcode sequence: GAGTCTGCCAGTATC), C0308 (barcode sequence: TATAGAACGCCAGGC), C0309 (barcode sequence: TGCCTATGAAACAAG) or C0310 (barcode sequence: CCGATTGTAACAGAC). Viable cells were sorted as CD45.2$^+$Thy1.2$^+$CD4$^-$CD8tetramer$^+$. Cells were sorted using the BD FACSAria Fusion flow cytometer (BD Biosciences). For TCR/scRNA-seq, 2,000–50,000 cells were sorted in 300 μl of PBS + 2% FCS and kept at 4 °C. Cells were then counted and resuspended at an adequate concentration for loading into the 10x chip. Gene expression and TCR libraries were generated using the Chromium Single Cell 5′ Library and V(D)J Reagent Kit (10x Genomics) according to manufacturer's recommendations. Then, 20,000 cells per sample were loaded into each channel of the Chromium Chip, and recommendations were followed assuming targeted cell recovery of 2,000–10,000 cells. 10x Genomics single-cell gene expression libraries were quantified using the Qubit dsDNA HS Assay Kit (Thermo Fisher Scientific) and profiled using the Bioanalyzer High Sensitivity DNA Kit (Agilent Technologies). Gene expression libraries were pooled and sequenced on the NovaSeq 6000 (Illumina) system to generate around 200 million paired-end reads per library in a 28 × 10 × 10 × 90 bp configuration. TCR libraries were pooled and sequenced on the NovaSeq 6000 (Illumina) system to generate 40–50 million paired-end reads per library in a 28 × 10 × 10 × 90 bp configuration. Feature barcode libraries were pooled and sequenced on the NovaSeq 6000 (Illumina) system to generate 15–20 million paired-end reads per library in a 28 × 10 × 10 × 90 bp configuration. For the MC38 pan-leukocyte single-cell dataset (Fig. 1), we sorted live, CD45$^+$ cells from single-cell suspensions of tumours from 3 mice using the FACSAria (BD Biosciences) system. Moreover, T cells from four mice were isolated (live, CD45$^+$TCRβ$^+$). All of the subsequent sequencing steps were performed as described previously[54].

Analysis of mouse scRNA/TCR-seq samples

scRNA-seq FASTQ files were processed using the count utility from CellRanger (10x Genomics) using a custom reference generated from GENCODE M15 gene annotations and GRCm38/mm10. Single-cell TCR-seq fastq files were processed using the VDJ utility from CellRanger

(10x Genomics). Multiplexed samples and antibody-specific barcodes were parsed using a wrapper to the DemuxEM package[68]. The resulting UMI counts were read into Seurat[69], and TCR information was added to the metadata.

Cells were filtered for singlets marked by DemuxEM and cells with more than 500 genes expressed and less than 5% of reads from mitochondrial genes. T-cell-receptor-encoding genes (*Tra*, *Trd* and *Trj*) were removed from the Seurat object to remove bias from TCR usage. Data were log-normalized using the NormalizeData function from Seurat. The top 2,000 variable features were selected using FindVariableFeatures, and the data were scaled using ScaleData. Principal components (PCs) were calculated using RunPCA, and nearest neighbours were identified using FindNeighbors with 30 PCs. The data were clustered to a resolution using FindClusters with 30 PCs. UMAPs were generated based on 30 PCs using RunUMAP.

The first of two replicate experiments was clustered with resolution 0.8, and contaminating clusters were removed, including cells with expression of *Cd19*/*Ms4a1* (B cells) or *CD74* (myeloid cells). Data from the second experiment was clustered to a resolution of 0.8, and three contaminating clusters with high expression of NK markers (*Fcer1g*, *Klra7* and *Klra1*), myeloid cell markers (*Cd74*) or CD4+ T cell markers (*Cd40lg*) were removed. The data were then clustered to a resolution of 1.8 to remove two additional clusters with high expression of *Cd74* and heat shock protein genes, respectively. The two experiments were then combined, and one sample with a low number of genes detected was removed due to quality concerns. Only RPL18-specific cells were retained, and the data were split into 13,576 cells from the tumour and 6,615 cells from the dLN. The two experiments were integrated with Harmony for tumour and dLN separately[70] (R package v.0.1.0; https://portals.broadinstitute.org/harmony/). After quality control, we performed dimensionality reduction using UMAP on a total of 20,191 single cells (6,791 control; 10,641 IL-27; 2,759 anti-IL-27) with a mean of 3,163 detectable genes per cell.

For TCR analyses, the mean hill diversity index was calculated using alphaDiversity from alakazam[71] with a diversity order (*q*) of 1, a minimum of 100 cells per sample and 100 bootstraps. Statistical comparisons were done using the Kruskal–Wallis rank-sum tests from the kruskal.test function from the stats package in R[72]. The fraction of overlapping of clones between tumour and lymph node was calculated as the number of unique clones found in both tumour and lymph node in an animal divided by the total number of unique clones of the union in both tumour and lymph node.

cNMF was run with number of components from 4 to 20, 20 iterations and 2,000 genes[73]. In total, 17 components were chosen as this had the highest stability. Scores were normalized per cell. For differential expression analysis, the average expression of raw counts was calculated per animal. Samples with fewer than 200 cells were removed. Differentially expressed genes were calculated using edgeR and called as significant if $P < 0.05$ (refs. 74,75). Cytotoxic scores were calculated using AddModuleScore from Seurat with *Gzmb*, *Cd8a*, *Gzma*, *Nkg7*, *Prf1* and *Gzmk*. Correlation of cNMF scores with *Tox* expression or cytotoxic scores were performed using Pearson correlation analysis.

The MC38 CD45+ single-cell dataset was processed through the count utility from CellRanger (10x Genomics) using a custom reference generated from GENCODE M15 gene annotations and GRCm38/mm10. After reading the count matrix with the Seurat package, the data were log-normalized, most variable features were detected and data were scaled in the spaces of these features, all using the default parameters of the Seurat package. We then performed clustering (resolution 0.1) and nonlinear dimensionality reduction using 30 PCs as input, which were calculated based on the scaled data. *Ptprc*-negative (encoding CD45) cells were excluded and doublets were removed using the scDblFinder package (https://doi.org/10.12688/f1000research.73600.1). Final clustering after removal of doublets and cycling cells (identified using the CellCycleScoring method in Seurat) was performed using 15 PCs.

Similarly, 15 PCs were used as input for UMAP calculation. Cluster identities were assigned based on expression of established cell type markers: *Csf1r* (macrophages/monocytes), *Flt3* (DCs), *Cd8a* (CD8+ T cells), *Cd40lg* (CD4+ T cells), *Foxp3* (T_reg cells), *Ncr1* (NK cells) and *Cd79a* (B cells).

Preparation of mouse RPL18-specific CD8+ T cells and adoptive cell therapy

T cells were cultured in T cell medium prepared as follows: RPMI 1640, 10% FBS (HyClone), 1% GlutaMax (Gibco), 1% HEPES (Life Technologies), 1 nM sodium pyruvate (Life Technologies), 1% non-essential amino acids (Life Technologies), 100 U ml⁻¹ penicillin (Gibco) and 100 µg ml⁻¹ streptomycin-sulfate (Gibco). Mouse naive CD8+ T cells were purified from spleens of CD45.1 mice by negative selection with magnetic beads (EasySep, Stemcell Technologies). After purification, cells were >95% CD8+ T cells. Purified cells were cultured in T cell medium containing 10 ng ml⁻¹ IL-2 and CD3/CD28 Dynabeads (Life Technologies) at a 1:2 ratio of beads to cells. After 24 h, endogenous TCR was knocked out using sgTRAC and sgTRBC containing Cas9–RNPs and Lonza electroporation using buffer P4 as described previously[76]. Immediately after electroporation, cells were resuspended in medium and incubated at 37 °C for 5–30 min. Six-well plates were previously coated with retronectin at a concentration 20 µg ml⁻¹ in PBS at 4 °C overnight or 2 h at room temperature. Before or immediately after cell electroporation, the plates were washed with medium, and 1.5 ml of viral supernatant was dispensed per well of the six-well plate. Electroporated T cells were then added to each well, for a maximum of 4 million cells per well and a final concentration of 10 ng ml⁻¹ IL-2. The plate was then incubated at 37 °C for 5–10 min, sealed in plastic wrap and centrifuged at 800*g* for 90 min. A 2× volume of T cell medium containing 10 ng ml⁻¹ IL-2 was then added to each well and incubated at 37 °C for 48 h. Cells were grown in six-well plates for 1–4 days until adoptive cell transfer. Before adoptive cell transfer, Dynabeads were removed using magnets.

For virus generation, Phoenix cells were seeded at a concentration of 3.4 million cells per 10 cm dish in complete DMEM. Then, 24 h later, cells were transfected with 8 µg of retroviral construct (MSCV-based MIGR1 backbone) containing an RPL18-specific TCR + 2 µg of pCL-Eco plasmid (containing *gag*, *pol* and *env* for improved virus generation), using JetPrime reagent (Polyplus). The medium was changed 4 h after transfection. The viral supernatant was collected 48–72 h after transfection, centrifuged, filtered through 25 µm cellulose acetate filters and frozen at −80 °C.

For adoptive cell therapy studies, *Rag2*⁻/⁻ mice were inoculated with 1 million MC38 tumour cells. When tumours were ≥100 mm³, WT (non-transduced bulk CD8+ T cells) or RPL18-specific CD8+ T cells were transferred to tumour-bearing mice through tail-vein injection. Then, 1 day later, HTV was performed to induce systemic overexpression of IL-27. Tumours were processed for analysis after 10–11 days.

Repeated antigen stimulation of mouse OT-I CD8+ T cells in vitro

CD8+ T cells were purified from the spleens of OT-I mice by negative selection with magnetic beads (EasySep, Stemcell Technologies). After purification, cells were >95% CD8+ T cells. In each well of a 96-well plate, 0.5 million purified CD8+ T cells per ml were cultured in complete medium with or without 10 ng ml⁻¹ OVA_{257–264} (SIINFEKL) peptide in the presence or absence of 25 ng ml⁻¹ mouse IL-27 (R&D Systems). Complete medium is defined as follows: RPMI 1640, 10% FBS (Gibco), 2 mM L-glutamine (Life Technologies), 1% HEPES (Life Technologies), 1 nM sodium pyruvate (Life Technologies), 1% non-essential amino acids (Life Technologies), 100 U ml⁻¹ penicillin (Gibco), 100 µg ml⁻¹ streptomycin-sulfate (Gibco), 0.05 mM 2-mercaptoethanol (Sigma-Aldrich) and recombinant human IL-2 (10 ng ml⁻¹, Roche). For repeated peptide stimulation, 10 ng ml⁻¹ OVA_{257–264} peptide was added daily; cells were passaged and cultured with fresh complete medium containing cytokines as required. On day 5, cells were analysed by flow cytometry, killing assay, Seahorse assay, RNA-seq or ATAC–seq.

Article

CRISPR–Cas9 gene editing

Where applicable, *Streptococcus pyogenes* Cas9-based targeting sequences (20-mers) were identified using the IDT sgRNA design tool. Three guides per gene were selected and guide RNAs were ordered as Alt-R CRISPR-Cas9 sgRNAs from IDT. Cell transfection with Cas9–RNA complexes was performed as described previously[76,77].

In vitro stimulation of mouse T cells for pSTAT1 and pSTAT3 assay

Freshly isolated mouse T cells were seeded at a density of 200,000 cells per well in a 96-well plate in T cell medium. Alternatively, BW5147.3 T lymphoblasts (ATCC, TIB-47) were cultured in RPMI0 1640 medium supplemented with 10% heat-inactivated FBS and 2 mM L-glutamine. Cells were treated with increasing concentrations of IL-27 (2799-ML), IL-6 (406-ML), IL-2 (402-ML), IL-11 (418-ML), IL-12 (419-ML), IL-23 (1887-ML), OSM (495-MO) or LIF (8878-LF) from R&D Systems. After incubation, cells were lysed for detection of phosphorylated STAT1 (Tyr701) using the HTRF assay kit (63ADK026PEG, CisBio) and detection of phosphorylated STAT3 (Tyr705) using an electrochemiluminescence-based immunoassay (MSD, K150SVD).

Metabolic flux assays

Glycolysis and mitochondrial stress tests were conducted using the Seahorse XFe96 Analyzer (Agilent Technologies) according to manufacturer's instructions. In total, 300,000 T cells per well were added to Seahorse XFe96 cell culture microplates (Agilent, 103794-100) and placed in a non-CO_2 incubator for 1 h before running the assay. The glycolysis stress test (Agilent, 103020-100) was conducted in XF base medium (Agilent Technologies, 102353-100) (pH 7.4) supplemented with 2 mM glutamine; final concentrations of 10 mM glucose, 1 µM oligomycin and 50 mM 2-DG (2-deoxy-D-glucose) were used for the injected compounds. The mitochondrial stress test (Agilent, 103015-100) was conducted in XF base medium (pH 7.4) supplemented with 2 mM glutamine, 1 mM sodium pyruvate and 10 mM glucose; final concentrations of 1.5 µM oligomycin, 1.5 µM FCCP (carbonyl cyanide *p*-trifluoro methoxyphenylhydrazone), 0.5 µM rotenone and 0.5 µM antimycin A were used for the injected compounds. After three baseline measurements, preloaded compounds were injected into the wells and the extracellular acidification rate and oxygen consumption rate were measured in real-time every 6–7 min. Data were collected using Agilent Seahorse Wave v.2.6.3 software.

Human CMV-specific CD8+ T cell assays

Primary human CD8+ T cells were isolated by positive selection from buffy coats using the StraightFrom Buffy Coat CD8+ MicroBead Kit (Miltenyi Biotec), according to manufacturer's instructions. Residual red blood cells were lysed before culture. Cells were plated at an initial concentration of 1 million cells per ml of stimulation medium. Unless otherwise noted, stimulation medium consisted of PRIME-XV T Cell CDM medium (Irvine Scientific) supplemented with IL-7 (Miltenyi Biotec) at 25 ng ml⁻¹ and IL-15 (Miltenyi Biotec) at 50 ng ml⁻¹. T cell TransAct (Miltenyi Biotec) was added to the cultures at a 1:100 dilution. T cell medium was prepared using the following ingredients: RPMI 1640 (11875093; Gibco), 10% FBS (SH30071.03; Hyclone), 2 mM L-alanyl-L-glutamine (GlutaMAX; Gibco), 1 mM sodium pyruvate (Gibco), 0.1 mM nonessential amino acids (Gibco), 55 µM 2-mercaptoethanol (Gibco), 100 U ml⁻¹ penicillin, 100 µg ml⁻¹ streptomycin (Gibco) and 10 mM HEPES (Gibco). The medium was sterilized through a 0.22 µm filter. T cells were cultured for 36–48 h before electroporation and co-transfection with sgTRAC- and sgTRBC-containing Cas9–RNPs, together with 4 µg of nanoplasmid encoding CMV A2/pp65$_{495-503}$-specific TCR6-2 as described previously[77]. The culture volume was expanded to maintain cells at 1 million cells per ml over the course of the culture. Then, 5 days later, cells were washed and cultured in complete medium (RPMI 1640, 10% FBS (Gibco), 1% 2 mM L-glutamine (Life Technologies), 1% HEPES (Life Technologies), 1% 100 nM sodium pyruvate (Life Technologies), 1% non-essential amino acids (Life Technologies), 100 U ml⁻¹ penicillin (Gibco), 100 µg ml⁻¹ streptomycin-sulfate (Gibco), 0.05 mM 2-mercaptoethanol (Sigma-Aldrich)) and recombinant human IL-2 (10 ng ml⁻¹, Roche).

Human T cell activation cultures comprised CRISPR-engineered T cells and an HLA-A*02:01+ target cell line obtained from the Fred Hutchinson International Histocompatibility Working Group. Peptide at 0.1–1 ng ml⁻¹ and target cells (adjusted to achieve a 1:1 effector-to-target ratio) were added every day for 5 days in the presence or absence of IL-27 at 25 ng ml⁻¹. Conditions without peptide were included as controls. Then, 3–5 days later, cells were collected and analysed by flow cytometry or RNA was extracted with RNeasy Mini Kit (Qiagen) for RNA-seq.

CD4 T cell preparation for bulk RNA-seq

Using MC38 tumour-bearing FOXP3–GFP mice, cells from lymph node digests were enriched for CD4+ T lymphocytes by negative selection using the EasySep mouse CD4+ T cell Isolation Kit (StemCell Technologies, 19852) and cells from tumour digests were enriched for CD45+ cells by positive selection with the EasySep mouse CD45+ positive cell isolation kit (StemCell Technologies, 18945). The enriched lymphocytes were subsequently stained and FACS-sorted for bulk RNA-seq. Cells were stained for surface antigens (CD8, CD45.2, Thy1.2, CD4). Viable T cells from tumour and dLN were sorted as CD45.2+Thy1.2+CD4+CD8−GFP+ (T_{reg}) or CD45.2+Thy1.2+CD4+CD8−GFP− (CD4+ T_{conv} cells). Cells were sorted using the BD FACSAria Fusion flow cytometer (BD Biosciences). In total, 2,000–33,000 cells were sorted into 300 µl of PBS + 2% FCS, pelleted by centrifugation and lysed in RLT buffer. RNA was extracted using the RNeasy Mini Kit (Qiagen) for RNA-seq.

Bulk RNA-seq of experimental samples

Total RNA was quantified using the Qubit RNA HS Assay Kit (Thermo Fisher Scientific) and the quality was assessed using RNA ScreenTape on the 4200 TapeStation (Agilent Technologies). For mouse CD4+ T and human CD8+ T cells, libraries were generated from 2 ng of total RNA using the Smart-Seq V4 Ultra Low Input RNA Kit (Takara); 150 pg of cDNA was used to make the sequencing libraries using the Nextera XT DNA Sample Preparation Kit (Illumina). For library generation from OT-I T cells, the Truseq Stranded mRNA kit (Illumina) was used with an input of 100–1,000 ng of total RNA. Libraries were quantified with Qubit dsDNA HS Assay Kit (Thermo Fisher Scientific) and the average library size was determined using D1000 ScreenTape on 4200 TapeStation (Agilent Technologies). Libraries were pooled and sequenced on NovaSeq 6000 (Illumina) system to generate 30 million single-end 50 bp reads for each sample.

RNA-seq data from human CD8+ T cells, OT-I T cells and mouse CD4+ T cells were processed using the BioConductor package HTSeqGenie[78] as follows: first, reads with low nucleotide qualities (70% of bases with quality <23) or matches to rRNA and adapter sequences were removed. The remaining reads were aligned to the reference genome (human: GRC38.p10, mouse: GRCm38.p5) using GSNAP[79] (version '2013-10-10-v2', allowing a maximum of two mismatches per 75 base sequence (parameters: '-M 2 -n 10 -B 2 -i 1 -N 1 -w 200000 -E 1 --pairmax-rna=200000 --clip-overlap'). Transcript annotation was based on the Gencode genes database (human: GENCODE 27, mouse: GENCODE M15). To quantify gene expression levels, the number of reads mapping unambiguously to the exons of each gene was calculated.

For mouse CD4+ T cells, genes were filtered for expression in at least three cells. Counts were normalized to CPM using edgeR[74]. Differentially expressed genes were calculated using edgeR and called as significant if $P < 0.01$. Expression values for heat maps were scaled using the scale_rows function from the pheatmap package[80]. Heatmaps were constructed using ComplexHeatmap[81].

For human CD8+ T cells and OT-I T cells, differentially expressed genes between IL-27-treated and untreated cells within a donor were determined

on trimmed mean of *M*-value-normalized counts using the R package limma voom () with the following design formula: *y ~ donor + treatment*. Moderated *t*-statistics were used as input into the fast Gene Set Enrichment Analysis Bioconductor package[82], and estimated *P* values were adjusted based on the Benjamini–Hochberg false-discovery rate. Large gene set databases often provide gene sets that are too broad or even irrelevant to an isolated cell population such as activated CD8 T cells; we therefore used a curated set of custom, T cell state and pathway activation signatures as follows: cytotoxic (custom, including *GZMA*, *GZMB*, *GZMH*, *GZMK*, *NKG7*, *PRF1*); CD8_NaiveLike, CD8_EffectorMemory, CD8_Early-Activ, CD8_Tpex, CD8_Tex (ProjecTILs, CD8 subsets only[40]); and EGFR, hypoxia, JAK–STAT, MAPK, NFκB, PI3K, TGFβ, TNFα, TRAIL, VEGF, WNT, p53 (PROGENy, top 100 upregulated per set[83]).

ATAC–seq library preparation, sequencing and analysis
ATAC–seq libraries were generated from fresh cells using the ATAC-Seq Kit (Active Motif, 53150). Libraries were quantified using the Qubit dsDNA HS Assay Kit (Thermo Fisher Scientific) and profiled using the D5000 ScreenTape on TapeStation 4200 (Agilent Technologies). Libraries were pooled and sequenced on the Illumina sequencer to generate paired-end 50 bp reads. To analyse ATAC–seq data, adapters were first trimmed with Cutadapt. Reads were aligned with Bowtie2 to the reference genome GRCm38. PCR duplicates were flagged by MarkDuplicates from Picard. SAMTools was used to filter out duplicated, unpaired and mitochondrial reads. BAM files were converted to paired bed files using Bedtools bamtobed -bedpe, after which reads were shifted by 4 or 5 bp to account for the cutting bias introduced by Tn5. MACS2 callpeak was used for peak calling with a *P*-value threshold of 0.01. Peaks were filtered for GRCm38 blacklist regions. Diffbind was used for summarizing open chromatin regions across all of the samples and performing differential analysis. Motif enrichment within differentially accessible regions was performed using AME.

Tumour RNA-seq and survival analysis for IMvigor210, IMvigor211 and OAK studies
mUC samples were collected from cohort 2 of IMvigor210[84], a single-arm phase 2 study investigating atezolizumab in patients with mUC (NCT02108652) and IMvigor211 (NCT02302807), a randomized open-label phase 3 trial of mUC[85]. mNSCLC samples were collected from OAK (NCT02008227), a randomized, open-label phase 3 study comparing atezolizumab versus chemotherapy[86]. In all studies, the patients were treated with atezolizumab as a second-line or higher treatment. Whole-transcriptome data were generated as described in the referenced studies.

To identify biology associated with *IL27*/*EBI3* expression, we grouped patients based on the upper quartiles of *IL27* and *EBI3*. Differentially expressed genes between *IL27*high and *EBI3*high versus *IL27*low and *EBI3*low were determined using the R package limma[87] (Bioconductor). Gene set enrichment analysis (GSEA) was performed on the results of the differential gene expression analysis using the QuSAGE analysis and the BostonGene gene sets[88]. The differentially expressed gene list was ranked according to the combined log-transformed fold change and adjusted *P* value and used as an input for GSEA. Histologically defined immune phenotypes were assigned to individual samples as described previously[89].

Probability of OS was estimated using the Kaplan–Meier method. Patients were grouped based on treatment arm and *IL27*/*EBI3* as described above. For OS analysis, data were censored for patients who were alive at the time of last contact. HRs and 95% CIs for OS were estimated using a Cox regression model. *P* values were calculated using the log-rank test.

Statistical analysis
Unless otherwise stated (for example, for RNA-seq analysis), Graph-Pad Prism 10 was used for data analysis and representation. Statistical analyses were performed as described in figure legends. All tests were two-sided with a significance threshold of 0.05. Summary line graphs, bar charts and associated datapoints represent the mean values of data; the error bars indicate the s.e.m.

Reporting summary
Further information on research design is available in the Nature Portfolio Reporting Summary linked to this article.

Data availability
The results shown here are in whole or part based on data generated by the TCGA Research Network (http://cancergenome.nih.gov/). Normalized and batch-adjusted RNA-seq data were obtained from the UCSC Xenabrowser (https://xenabrowser.net/datapages/). Additional publicly available RNA-seq datasets used in this study include GSE91061 (nivolumab-treated non-ocular melanoma biopsies)[48], GSE168846 (untreated mouse syngeneic tumours)[15] and GSE199045 (resting mouse CD8+ T cells)[90]. Normalized gene expression data and associated sample metadata were extracted directly from Gene Expression Omnibus (https://www.ncbi.nlm.nih.gov/geo/). RNA-seq data from the IMvigor210, IMvigor211 and OAK studies are available from the European Genome-Phenome Archive (EGA) under accession numbers EGAS00001002556, EGAD00001007703, EGAD00001008391 and EGAS50000000497. Bulk and single-cell raw sequencing data from mouse samples are available from the ArrayExpress database under the following accession IDs: ATAC–seq analysis of OT-I T cells (E-MTAB-14584); bulk RNA-seq analysis of CD4+ T cells (E-MTAB-14581); bulk RNA-seq analysis of OT-I T cells (E-MTAB-14580); scRNA-seq analysis of immune cells (E-MTAB-14590); scRNA-seq (expression and TCR sequencing) analysis of CD8+ T cells (E-MTAB-14601). Bulk sequencing data for human T cells are available from the EGA under accession number EGAS50000000694. Biological materials are available on request from the corresponding author. Source data are provided with this paper.

Code availability
No new algorithms were developed for this Article. Processed data and analysis code is available through the Open Science Framework (OSF) project under ID f6re4.

61. Collison, L. W. et al. The inhibitory cytokine IL-35 contributes to regulatory T-cell function. *Nature* **450**, 566–569 (2007).
62. Haribhai, D. et al. Regulatory T cells dynamically control the primary immune response to foreign antigen. *J. Immunol.* **178**, 2961–2972 (2007).
63. Lin, W. et al. Regulatory T cell development in the absence of functional Foxp3. *Nat. Immunol.* **8**, 359–368 (2007).
64. Hogquist, K. A. et al. T cell receptor antagonist peptides induce positive selection. *Cell* **76**, 17–27 (1994).
65. Chen, Q. et al. Development of Th1-type immune responses requires the type I cytokine receptor TCCR. *Nature* **407**, 916–920 (2000).
66. Clausen, B. E., Burkhardt, C., Reith, W., Renkawitz, R. & Förster, I. Conditional gene targeting in macrophages and granulocytes using LysMcre mice. *Transgenic Res.* **8**, 265–277 (1999).
67. Schraml, B. U. et al. Genetic tracing via DNGR-1 expression history defines dendritic cells as a hematopoietic lineage. *Cell* **154**, 843–858 (2013).
68. Gaublomme, J. T. et al. Nuclei multiplexing with barcoded antibodies for single-nucleus genomics. *Nat. Commun.* **10**, 2907 (2019).
69. Stuart, T. et al. Comprehensive integration of single-cell data. *Cell* **177**, 1888–1902 (2019).
70. Korsunsky, I. et al. Fast, sensitive and accurate integration of single-cell data with Harmony. *Nat. Methods* **16**, 1289–1296 (2019).
71. Gupta, N. T. et al. Change-O: a toolkit for analyzing large-scale B cell immunoglobulin repertoire sequencing data. *Bioinformatics* **31**, 3356–3358 (2015).
72. R Core Team (2021): R: A language and environment for statistical computing (R Foundation for Statistical Computing, 2021); www.R-project.org/.
73. Kotliar, D. et al. Identifying gene expression programs of cell-type identity and cellular activity with single-cell RNA-seq. *eLife* **8**, e43803 (2019).
74. Robinson, M. D., McCarthy, D. J. & Smyth, G. K. edgeR: a Bioconductor package for differential expression analysis of digital gene expression data. *Bioinformatics* **26**, 139–140 (2010).
75. Lun, A. T. L., Chen, Y. & Smyth, G. K. It's DE-licious: a recipe for differential expression analyses of RNA-seq experiments using quasi-likelihood methods in edgeR. *Methods Mol. Biol.* **1418**, 391–416 (2016).

76. Oh, S. A., Seki, A. & Rutz, S. Ribonucleoprotein transfection for CRISPR/Cas9-mediated gene knockout in primary T cells. *Curr. Protoc. Immunol.* **124**, e69 (2019).
77. Oh, S. A. et al. High-efficiency nonviral CRISPR/Cas9-mediated gene editing of human T cells using plasmid donor DNA. *J. Exp. Med.* **219**, e20211530 (2022).
78. Pau, G. & Reeder, J. HTSeqGenie: a NGS analysis pipeline. R package version 4.32.0 (2023); https://bioconductor.org/packages/HTSeqGenie.
79. Wu, T. D., Reeder, J., Lawrence, M., Becker, G. & Brauer, M. J. GMAP and GSNAP for genomic sequence alignment: enhancements to speed, accuracy, and functionality. *Methods Mol. Biol.* **1418**, 283–334 (2016).
80. Kolde, R. pheatmap: pretty Heatmaps. R package version 1.0.12 (2019); CRAN.R-project.org/package=pheatmap.
81. Gu, Z., Eils, R. & Schlesner, M. Complex heatmaps reveal patterns and correlations in multidimensional genomic data. *Bioinformatics* **32**, 2847–2849 (2016).
82. Korotkevich, G. et al. Fast gene set enrichment analysis. Preprint at *bioRxiv* https://doi.org/10.1101/060012 (2021).
83. Holland, C. H., Szalai, B. & Saez-Rodriguez, J. Transfer of regulatory knowledge from human to mouse for functional genomics analysis. *Biochim. Biophys. Acta* **1863**, 194431 (2020).
84. Rosenberg, J. E. et al. Atezolizumab in patients with locally advanced and metastatic urothelial carcinoma who have progressed following treatment with platinum-based chemotherapy: a single-arm, multicentre, phase 2 trial. *Lancet* **387**, 1909–1920 (2016).
85. Powles, T. et al. Atezolizumab versus chemotherapy in patients with platinum-treated locally advanced or metastatic urothelial carcinoma (IMvigor211): a multicentre, open-label, phase 3 randomised controlled trial. *Lancet* **391**, 748–757 (2018).
86. Rittmeyer, A. et al. Atezolizumab versus docetaxel in patients with previously treated non-small-cell lung cancer (OAK): a phase 3, open-label, multicentre randomised controlled trial. *Lancet* **389**, 255–265 (2017).
87. Ritchie, M. E. et al. limma powers differential expression analyses for RNA-sequencing and microarray studies. *Nucleic Acids Res.* **43**, e47 (2015).
88. Bagaev, A. et al. Conserved pan-cancer microenvironment subtypes predict response to immunotherapy. *Cancer Cell* **39**, 845–865 (2021).
89. Li, X. et al. Automated tumor immunophenotyping predicts clinical benefit from anti-PD-L1 immunotherapy. *J. Pathol.* **263**, 190–202 (2024).
90. Huseni, M. A. et al. CD8^{+} T cell-intrinsic IL-6 signaling promotes resistance to anti-PD-L1 immunotherapy. *Cell Rep. Med.* **4**, 100878 (2023).

Additional information
Supplementary information The online version contains supplementary material available at https://doi.org/10.1038/s41586-024-08510-w.
Correspondence and requests for materials should be addressed to Sören Müller or Nathaniel R. West.
**Peer review information** *Nature* thanks Christoph Garbers, Sebastian Kobold and the other, anonymous, reviewer(s) for their contribution to the peer review of this work.
Reprints and permissions information is available at http://www.nature.com/reprints.
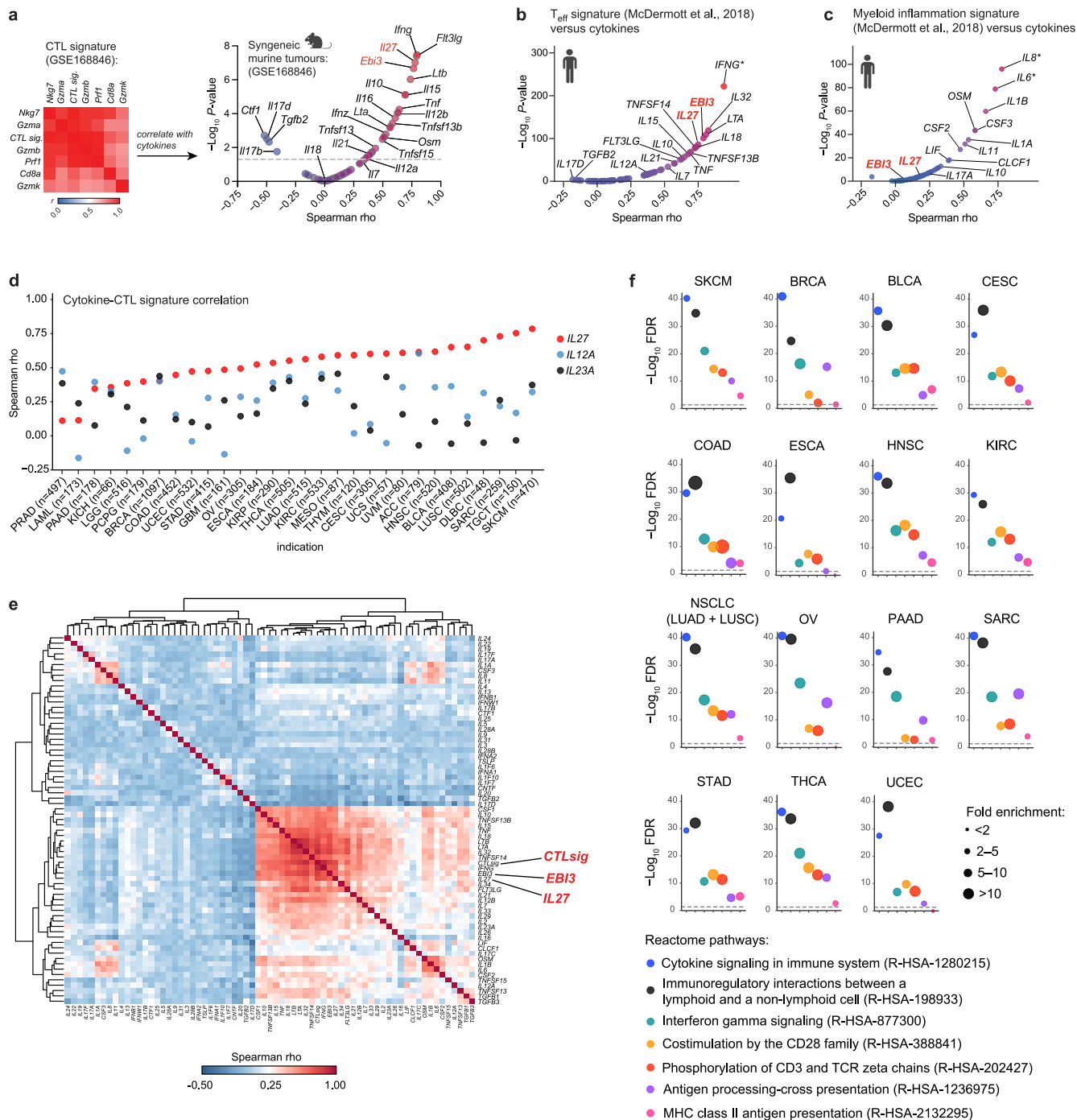
Extended Data Fig. 1 | Analysis of IL-27 expression in human and murine tumours. (**a**) Spearman correlation of CTLsig and cytokine gene expression in n = 33 murine tumour samples representing 11 syngeneic models (reanalysed from GSE168846[15]). (**b**–**c**) Spearman correlation between cytokine expression and previously published[17] T effector (**b**) or myeloid inflammation (**c**) signatures in the human melanoma (SKCM) TCGA dataset. Asterisks indicate genes that are components of the corresponding signatures. The mouse and human icons in **a**–**c** were created using BioRender. (**d**) Spearman correlation of the human CTLsig with *IL27, IL12A* or *IL23A* across solid tumour types from TCGA. (**e**) Spearman correlation matrix and hierarchical clustering of CTLsig and cytokine genes in the melanoma dataset of TCGA. (**f**) Gene ontology analysis of genes closely associated with *IL27* (top 500 genes based on Spearman correlation, per cancer type) in human solid tumour types from TCGA.

Reactome (v85, release date 5-25-2023) pathway enrichment was calculated using the Panther overrepresentation test (http://geneontology.org/). Statistical significance was calculated using Fisher's exact test with false discovery rate (FDR) correction. SKCM, skin cutaneous melanoma; BRCA, breast invasive carcinoma; BLCA, bladder urothelial carcinoma; CESC, cervical squamous cell carcinoma and endocervical adenocarcinoma; COAD, colon adenocarcinoma; ESCA, oesophageal carcinoma; HNSC, head and neck squamous cell carcinoma; KIRC, kidney renal clear cell carcinoma; NSCLC, non-small cell lung cancer, including lung adenocarcinoma and lung squamous cell carcinoma; OV, ovarian serous cystadenocarcinoma; PAAD, pancreatic adenocarcinoma; SARC, sarcoma; STAD, stomach adenocarcinoma; THCA, thyroid carcinoma; UCEC, uterine corpus endometrial carcinoma.
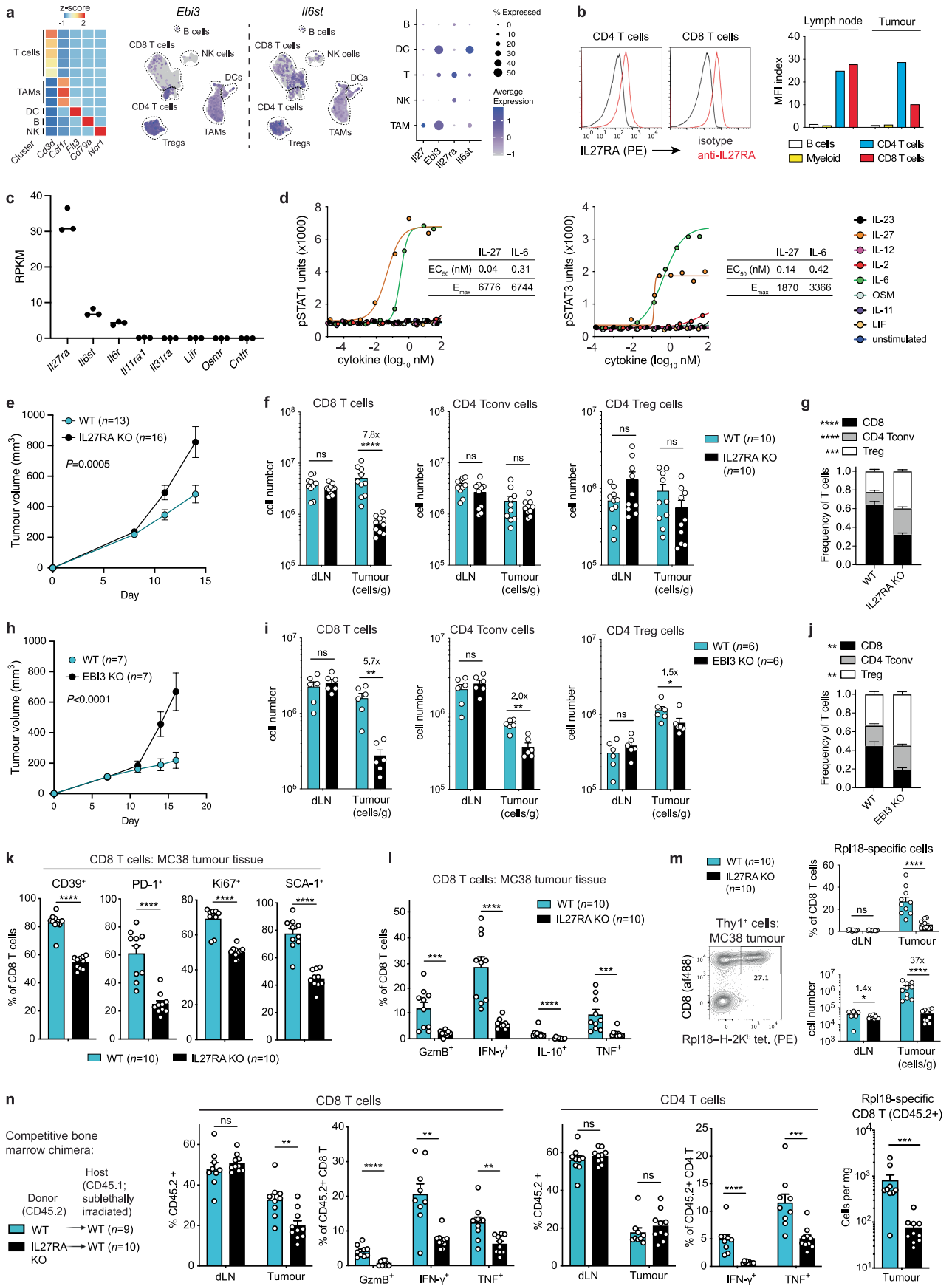
Extended Data Fig. 2 | See next page for caption.

**Extended Data Fig. 2 | Expression of IL-27 pathway components and functional impact of IL-27 signalling in the MC38 tumour model.** (**a**) Left: Relative average expression of indicated marker genes in clusters from Fig. 1b. Middle: UMAP as in Fig. 1b, coloured by expression of indicated markers. Right: expression of indicated markers in cell types given in Fig. 1b. (**b**) IL27RA surface expression on CD4+ and CD8+ T cells and mean fluorescence intensity normalized to isotype control in different CD45+ cell types (B cells, B220+Thy1−; myeloid cells, B220−Thy1−CD11b+) from MC38 tumour-bearing mice. (**c**) RNA expression of IL-6/gp130 family cytokine receptors in resting mouse CD8+ T cells (data reanalysed from GSE199045)[90]. (**d**) T cells isolated from healthy C57BL/6J mice were treated with increasing concentrations of the indicated cytokines for 30 min. Phosphorylated STAT1 (at Y701) and STAT3 (at Y705) were quantified in cell lysates. EC_{50} values are indicated as nM concentrations, while E_{max} values are reported as the maximal signal strength observed (in arbitrary units). (**e**–**m**) Mice were inoculated with MC38 cells and tumours and dLN were collected for flow cytometry analysis 15 days later. (**e**) Tumour growth in IL27RA KO mice and WT controls, compared using two-way ANOVA. (**f**) Abundance of FoxP3− CD4+ Tconv, FoxP3+CD4+ Treg, and CD8+ T cells in tumour and dLN of WT or IL27RA KO mice, compared using two-sided Mann-Whitney tests. (**g**) Frequencies of cell subsets among total tumour-infiltrating T cells from IL27RA KO or WT mice, compared using two-sided Mann-Whitney tests. (**h**) Tumour growth in EBI3 KO mice and WT controls, compared using two-way ANOVA. (**i**) Abundance of FoxP3−CD4+ Tconv, FoxP3+CD4+ Treg, and CD8+ T cells in tumour and dLN of WT or EBI3 KO mice, compared using two-sided Mann-Whitney tests. (**j**) Frequencies of cell subsets among total tumour-infiltrating T cells from EBI3 KO or WT mice, compared using two-sided Mann-Whitney tests. (**k**) Expression of the indicated markers in tumour-infiltrating CD8+ T cells from IL27RA KO or WT mice, compared using two-sided Mann-Whitney tests. (**l**) Expression of the indicated effector function markers in tumour-infiltrating CD8+ T cells from IL27RA KO or WT mice following restimulation with PMA and ionomycin, compared using two-sided Mann-Whitney tests. (**m**) Representative flow cytometry plot showing Rpl18−H-2Kb tetramer staining of CD8+ T cells among total tumour-infiltrating T cells, and quantification of Rpl18-specific CD8+ T cells in tumours and dLN (upper graph, frequencies among total CD8+ T cells; lower graph, absolute cell number). Groups compared using two-sided Mann-Whitney tests. (**n**) Competitive bone marrow chimeras in which bone marrow cells from CD45.2+ IL27RA KO or WT littermate controls were transferred to sublethally irradiated CD45.1 mice. Four weeks later, chimeric mice were inoculated with MC38 tumour cells and tissues were harvested for analysis after two weeks. Frequencies of CD45.2+CD8+ and CD45.2+CD4+ T cells are shown in dLN and tumour tissue, as well as frequencies of effector molecule expression among tumour-infiltrating CD45.2+ T cells. Absolute abundance (normalized to tumour weight) of CD45.2+ tumour-infiltrating Rpl18-specific CD8+ T cells is shown in the right panel. All data are representative of two independent studies. In all panels, statistical significance is indicated as follows: ns, not significant; *$P < 0.05$; **$P \leq 0.01$; ***$P \leq 0.001$; ****$P \leq 0.0001$.
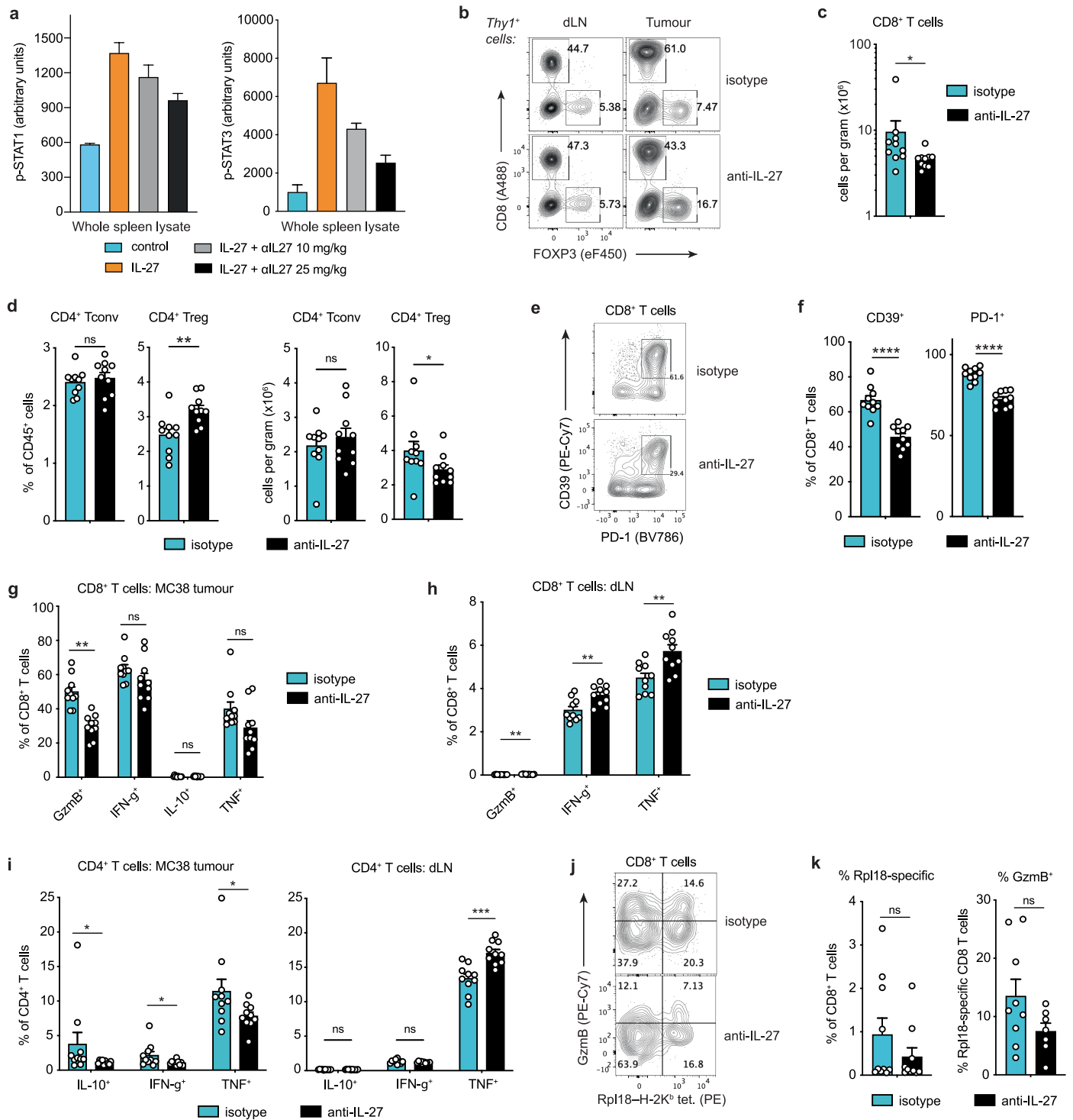
Extended Data Fig. 3 | Impact of IL-27 blockade on immune response to MC38 tumours. (**a**) C57BL/6J mice (*n* = 3 per group) were pretreated with IL-27 blocking antibody and challenged with intravenous injection of high-dose recombinant IL-27 (10 µg per mouse). Spleens were collected after 30 min and lysed for analysis of phosphorylated STAT1 (at Y701) and STAT3 (at Y705). (**b**–**k**) C57BL/6J mice were engrafted with MC38 cells and treated with isotype control or anti-IL-27 antibody. 15 days after tumour inoculation, tumours and draining lymph nodes (dLN) were collected for flow cytometry analysis. (**b**) Representative staining of CD8 and Foxp3 in total tumour-infiltrating T cells. (**c**) Total CD8+ T cells per gram of tumour. (**d**) Frequencies and absolute numbers of conventional and regulatory CD4+ T cells in tumour tissue. (**e**) Representative staining of PD-1 and CD39 on tumour-infiltrating CTL. (**f**) Frequency of PD-1+ and CD39+ cells among tumour-infiltrating CTL.

(**g**, **h**) Expression frequency of cytokines and GzmB in CD8+ T cells from (**g**) tumour tissue and (**h**) dLN following restimulation with PMA + ionomycin. (**i**) Expression frequency of cytokines in CD4+ T cells from tumour tissue and dLN following restimulation with PMA + ionomycin. (**j**) Representative staining of GzmB and Rpl18–H-2K^b tetramer among tumour-infiltrating CTL. (**k**) Frequency of Rpl18-specific cells among total CD8+ T cells, and GzmB+ cells among Rpl18-specific CD8+ T cells in dLN. All bar charts represent mean ± s.e.m. Panels **c**–**i**: *n* = 10 per group. Panel **k** (left): *n* = 10 per group. Panel **k** (right): *n* = 9 control and *n* = 7 anti-IL-27. Data are representative of two independent experiments. In all panels, groups were compared using two-sided Mann-Whitney tests with statistical significance indicated as follows: ns, not significant; *P < 0.05; **P ≤ 0.01; ***P ≤ 0.001; ****P ≤ 0.0001.
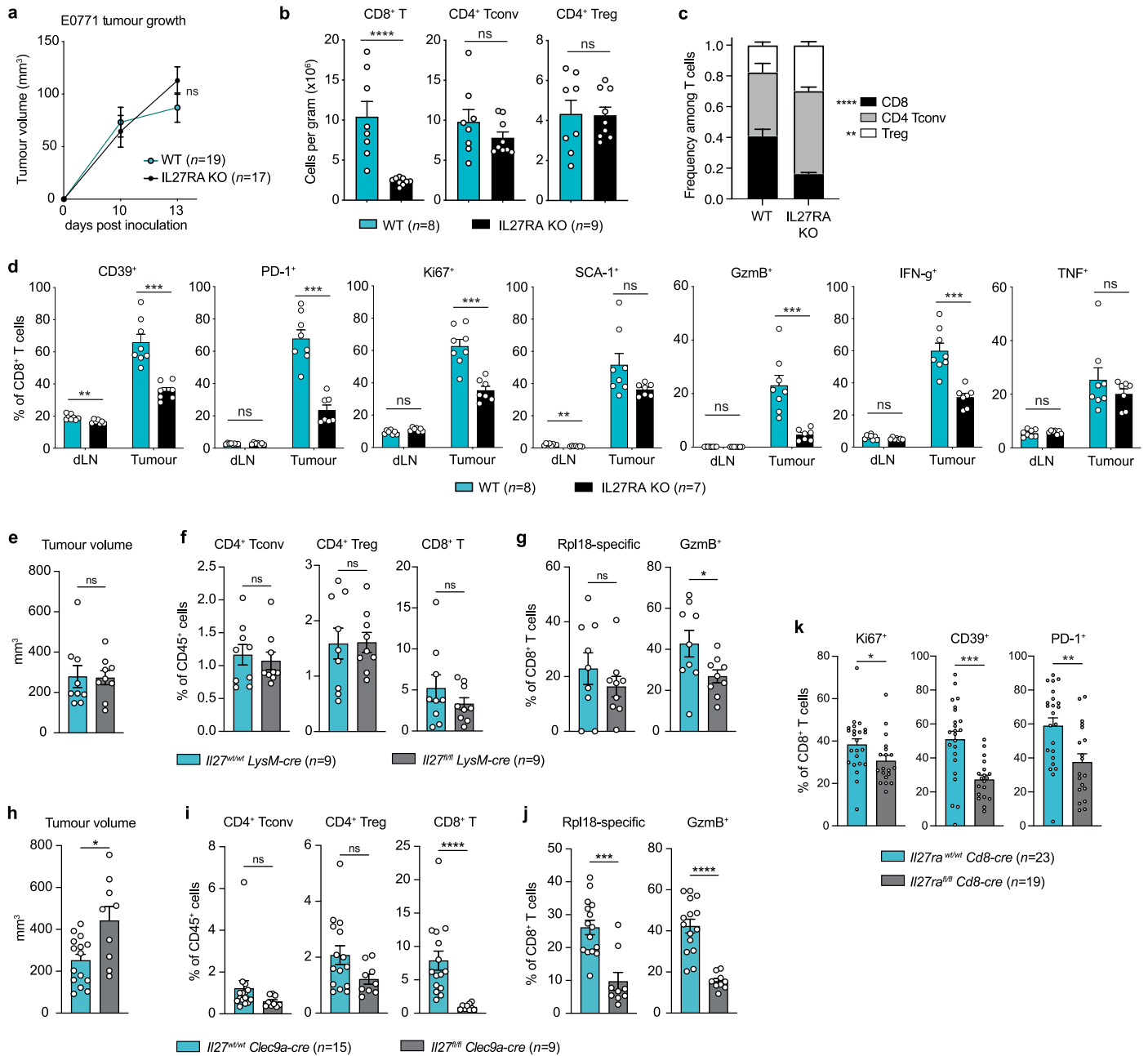
Extended Data Fig. 4 | Impact of IL-27RA or IL-27 deficiency on anti-tumour CTL. (a–d) IL27RA KO mice or WT littermate controls were inoculated in the mammary fat pad with E0771 cells. 15 days after tumour inoculation, tumours were collected for flow cytometry analysis directly or after restimulation with PMA and ionomycin for analysis of cytokine expression. **(a)** Tumour growth. Data pooled from two independent experiments and compared using two-way ANOVA. **(b)** Abundance (normalized to tumour weight) of FoxP3⁻CD4⁺ Tconv cells, FoxP3⁺CD4⁺ Treg cells, and CD8⁺ T cells in tumour tissue. **(c)** Frequency of CD4⁺ Tconv, Treg, and CD8⁺ T cells among total tumour infiltrating T cells. **(d)** Expression frequency of indicated markers in CD8⁺ T cells in tumour tissue and in dLN; $n = 8$ (WT) and $n = 9$ (IL27RA KO). In panels **b–d**, data are representative of two independent experiments. **(e–g)** $Il27^{fl/fl}$ $LysM$-cre mice or **(h–j)** $Il27^{fl/fl}$ $Clec9a$-cre mice and littermate controls were inoculated with MC38

tumour cells. Two weeks after inoculation, tumours were collected for flow cytometry analysis. Numbers of mice per group are as follows, pooled from two independent experiments: $n = 9$ ($Il27^{wt/wt}$ $LysM$-cre), $n = 9$ ($Il27^{fl/fl}$ $LysM$-cre), $n = 15$ ($Il27^{wt/wt}$ $Clec9a$-cre), and $n = 9$ ($Il27^{fl/fl}$ $Clec9a$-cre). **(e, h)** Tumour volumes at the study endpoint. **(f, i)** Frequency of FoxP3⁻CD4⁺ Tconv cells, FoxP3⁺CD4⁺ Treg cells, and CD8⁺ T cells in tumour tissue. **(g, j)** Frequency of GzmB expression and Rpl18-specific cells among tumour-infiltrating CTL. **(k)** Frequencies of activation marker expression among MC38 tumour-infiltrating CTL from mice with CTL-restricted IL-27RA deficiency or littermate controls ($n = 23$ $Il27ra^{wt/wt}$ and $n = 19$ $Il27ra^{flox/flox}$ mice), pooled from four independent experiments. In each panel, bar charts represent means ± s.e.m. compared using two-sided Mann-Whitney tests. ns, not significant; *$P < 0.05$; **$P ≤ 0.01$; ***$P ≤ 0.001$; ****$P ≤ 0.0001$.
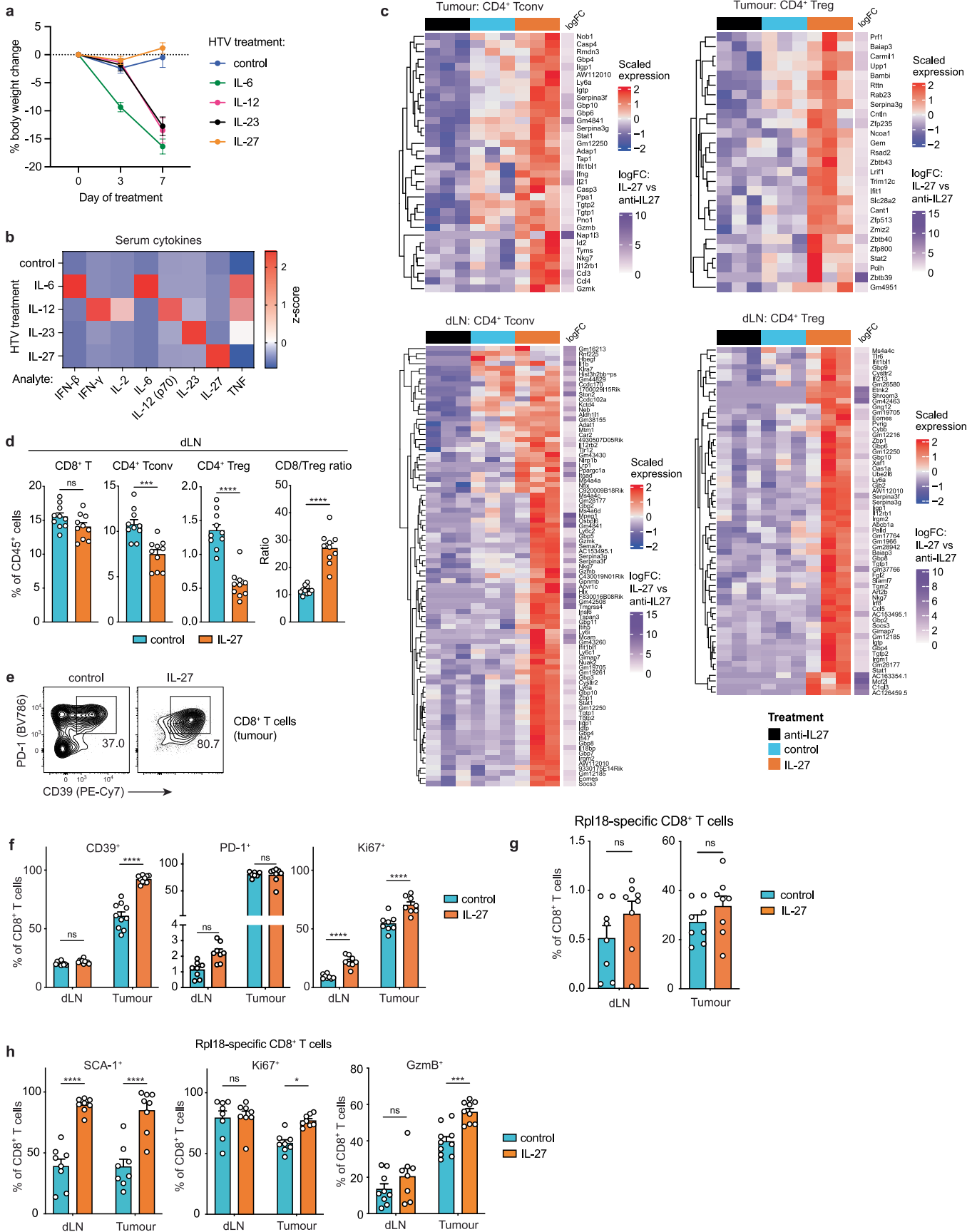
Extended Data Fig. 5 | See next page for caption.

Extended Data Fig. 5 | Immunostimulatory effects of inducible IL-27 overexpression in vivo. (**a**–**b**) Healthy C57BL/6J mice were treated once with HTV injection of control or cytokine-encoding plasmids. (**a**) Body weight change over the duration of sustained cytokine expression. Datapoints indicate mean ± s.e.m. from n = 4–5 mice per timepoint. (**b**) Mean serum cytokine concentration on day 7 (transformed to z-scores), measured by ELISA or multiplex Luminex assay. (**c**) C57BL/6J *Foxp3-GFP* reporter mice were engrafted with MC38 cells. When tumours reached 150 mm³ (day 0), mice were treated with IL-27 blocking antibody (anti-IL-27) or with HTV injection of control or IL-27-encoding (IL-27) plasmids. 7 days after treatment, CD4⁺ Tconv (GFP⁻) and CD4⁺ Treg (GFP⁺) were isolated by FACS from tumours and draining lymph nodes and processed for bulk RNAseq (n = 3 mice per group). Genes shown in heatmaps were significantly differentially expressed (adjusted P < 0.05) between anti-IL-27 and IL-27 groups based on limma-voom analysis with Benjamini-Hochberg correction. (**d**–**h**) C57BL/6J mice bearing established MC38 tumours were treated once with HTV injection of control or IL-27 encoding plasmids and T cells from tumours and dLN were analysed after 7 days (see Fig. 2). Data are representative of two independent experiments. (**d**) Frequencies of conventional CD4⁺ T cells, Treg cells, and CTL in dLN, along with associated CD8/Treg ratios. (**e**) Representative staining of PD-1 and CD39 in tumour-infiltrating CTL. (**f**) frequencies of PD-1, CD39, and Ki67 expression in CTL from tumour or dLN (n = 8–10 per group). (**g**) Rpl18-specific cells among CTL (n = 8 per group). (**h**) Frequency of SCA-1, Ki67, and GzmB expression among Rpl18-specific CTL (n = 8–10 per group). All bar-charts indicate mean ± s.e.m, compared using Mann-Whitney test, with P-values indicated as follows: ns, P > 0.05; *P < 0.05; **P ≤ 0.01; ***P ≤ 0.001; ****P ≤ 0.0001.
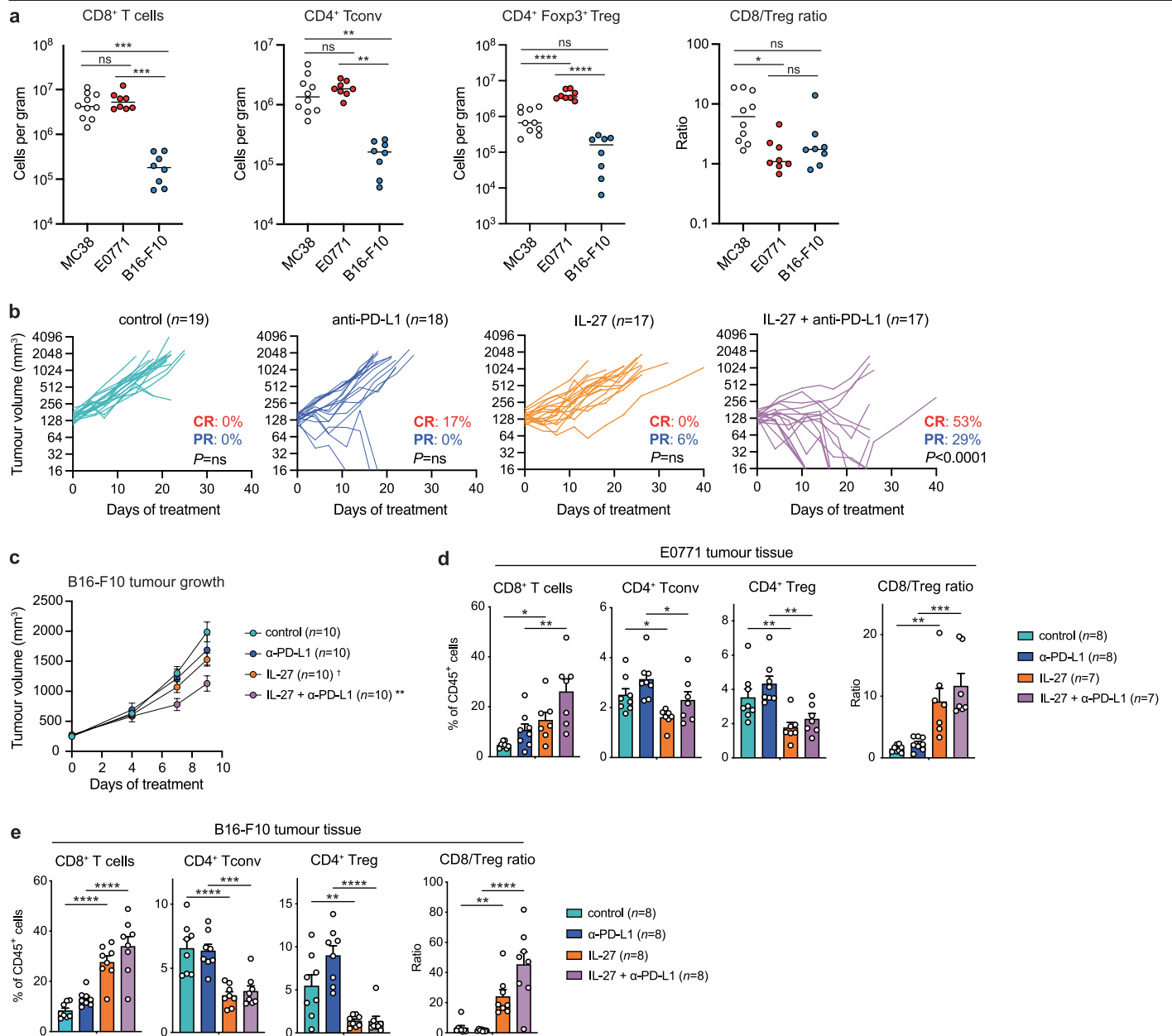
Extended Data Fig. 6 | IL-27R agonism synergizes with PD-L1 blockade.
(**a**) Comparison of T cell infiltration in different tumour models (MC38, E0771, and B16-F10). T cell abundance is expressed as absolute numbers per gram of tumour tissue. Data are representative of >3 independent experiments. (**b**–**e**) C57BL/6J mice were engrafted orthotopically with E0771 mammary tumour cells or subcutaneously with B16-F10 tumour cells. When tumours reached 150 mm³ (day 0), mice were treated once with HTV injection of control or IL-27-encoding plasmid in addition to biweekly isotype control or anti-PD-L1 antibody. (**b**) E0771 tumour growth (data pooled from two independent experiments). Response rates in treatment groups are compared to the control group and analysed by Fisher's exact test. (**c**) B16-F10 tumour growth. Treatment groups are compared to control group and analysed by 2-way ANOVA using a mixed-effects model with Holm-Sidak multiple testing correction; **P = 0.0045, †P = 0.0768 (at day 9). (**d**) FoxP3⁻CD4⁺ Tconv, FoxP3⁺CD4⁺ Treg, and CTL frequencies and the CD8/Treg ratio in E0771 tumours, compared using one-way ANOVA. *$P \leq 0.05$; **$P \leq 0.01$; ***$P \leq 0.001$. (**e**) FoxP3⁻CD4⁺ Tconv, FoxP3⁺CD4⁺ Treg, and CTL frequencies and the CD8/Treg ratio in B16-F10 tumours, compared using one-way ANOVA. **$P \leq 0.01$; ***$P \leq 0.001$; ****$P \leq 0.0001$. Data in panels **c**–**e** are representative of two independent experiments.
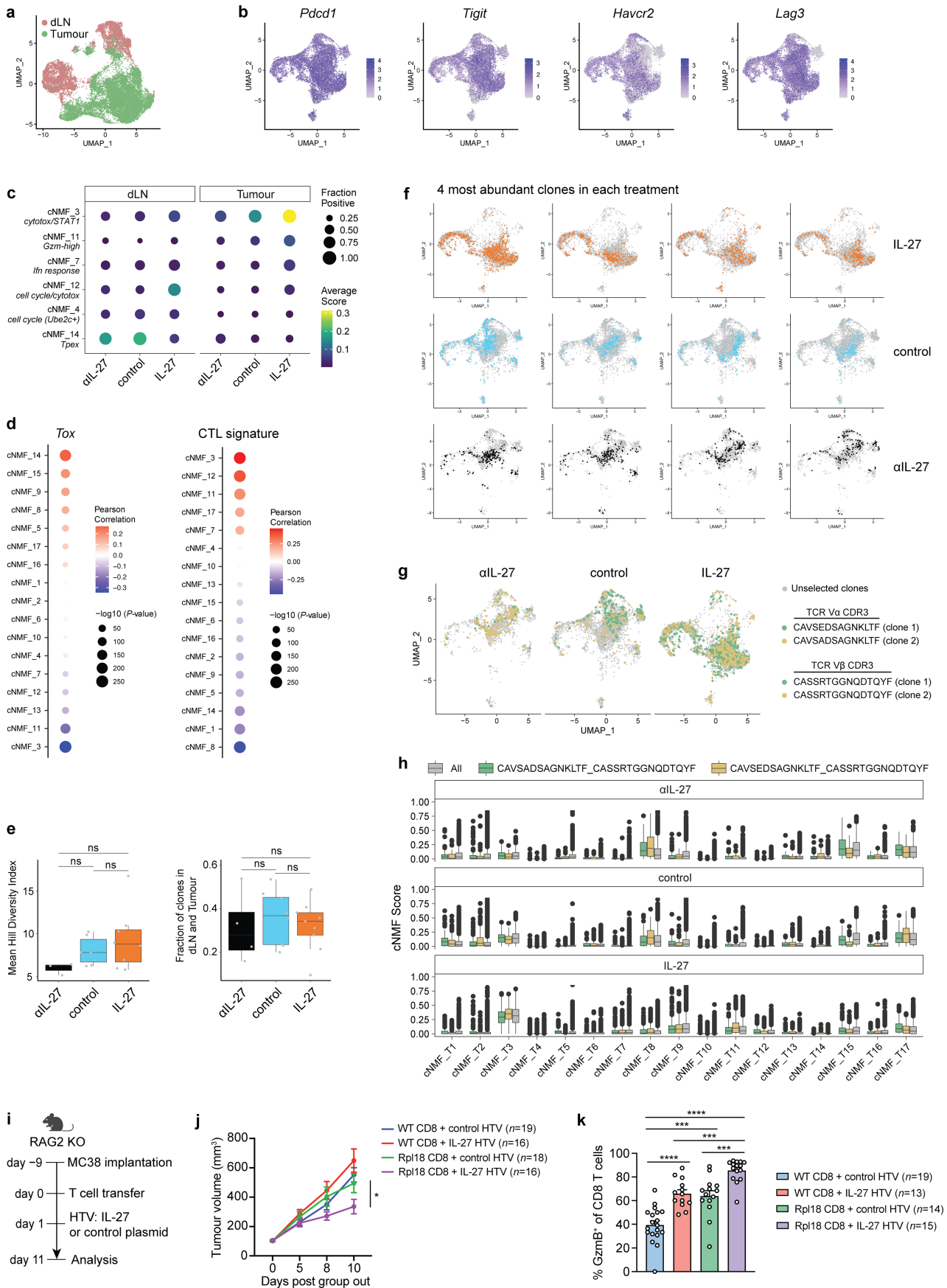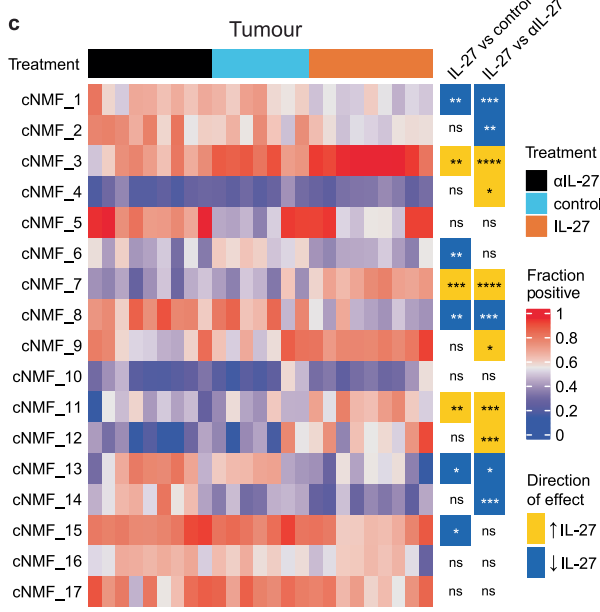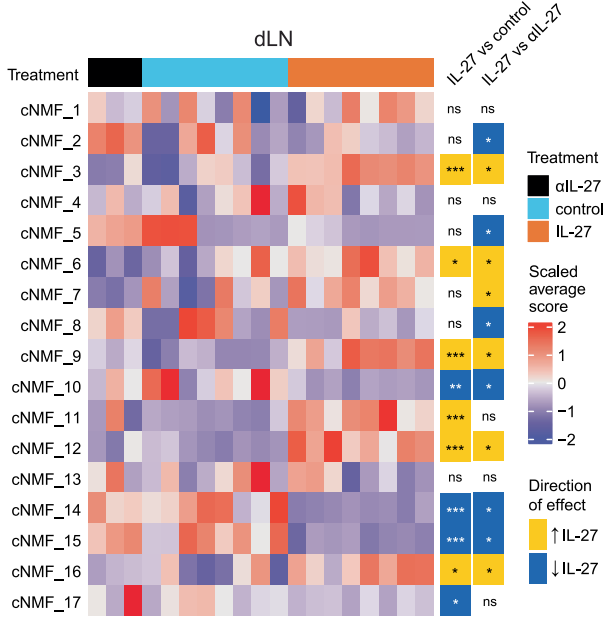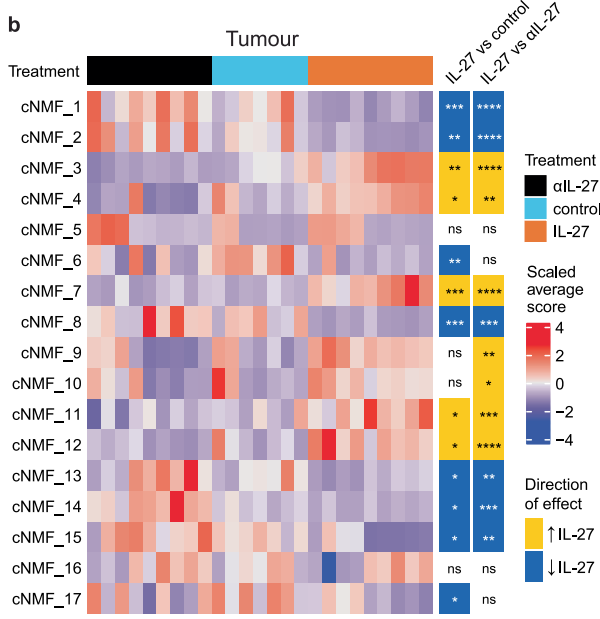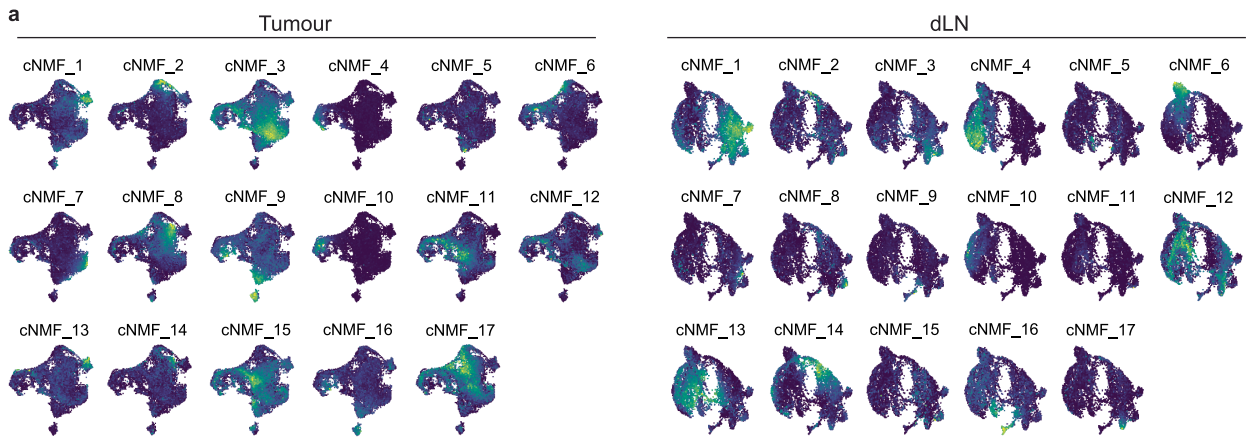
Extended Data Fig. 7 | See next page for caption.

Article

Extended Data Fig. 7 | Single-cell RNAseq analysis of Rpl18-specific CD8+ T cells. (**a**) UMAP of 20,191 Rpl18-specific CD8+ T cells from MC38 tumours and dLN of mice treated with anti-IL-27 blocking antibody (2,759 total cells), IL-27 overexpression by HTV injection of IL-27-encoding plasmid (10,641 total cells), or HTV injection of empty vector control plasmid in combination with isotype control antibody (control; 6,791 total cells). (**b**) UMAP plots showing expression of *Pdcd1*, *Tigit*, *Havcr2* and *Lag3* in tumour-infiltrating T cells. Colour intensity indicates normalized expression level in log(CPM/100 + 1) units. (**c**) Six cNMF programs highlighted in the tumour and dLN with their average cNMF score (colour) and fraction of cells with detectable cNMF program expression (size). (**d**) Dot plot illustrating Pearson correlation between cNMF programs and expression of *Tox* (left panel) or CTLsig (including *Gzmb*, *Cd8a*, *Gzma*, *Nkg7*, *Prf1*, *Gzmk*) in tumour-infiltrating T cells. Dot colour and size indicate correlation coefficients and *P*-values, respectively. (**e**, left panel) Clonal diversity (mean Hill diversity index) of tumour-infiltrating CTL based on TCR sequence. *P*-values are from Kruskal-Wallis test (ns, *P* > 0.05). Animals contributing <200 cells were excluded. (**e**, right panel) Fraction of clones found in both the dLN and tumour per animal. *P*-values are from Kruskal-Wallis test (ns, *P* > 0.05). (**f**) UMAP distribution of tumour-infiltrating T cells from the four most abundant clones (ranked from left to right) per treatment group. Grey points are cells from all expanded clones (clones with more than one cell). Coloured points are cells belonging to the top four clones for the given treatment group. (**g**) Tumour UMAP distribution of two clones found in all treatment groups and (**h**) distribution of cNMF scores. (**i**–**k**) *Rag2*−/− mice were engrafted with MC38 cells. When tumours reached a volume of approximately 100 mm³, 10⁶ bulk WT (non-transduced) CD8+ T cells or 10⁵ CD8+ T cells engineered to express an Rpl18-specific TCR (shown in panel **g**) were adoptively transferred by tail vein injection; one day later, mice received HTV injection of control or IL-27 encoding plasmid. After 11 days of treatment, tumour-infiltrating CD8+ T cells were isolated for flow cytometry analysis. Data are from one of two independent experiments. (**i**) Experimental schematic; the mouse icon was created using BioRender. (**j**) Tumour growth compared using two-way ANOVA with Holm-Sidak multiple comparisons test (*P < 0.05). (**k**) GzmB expression in TIL. Bars represent mean ± s.e.m., compared using one-way ANOVA with Holm-Sidak multiple comparisons test. ***P ≤ 0.001, ****P ≤ 0.0001.
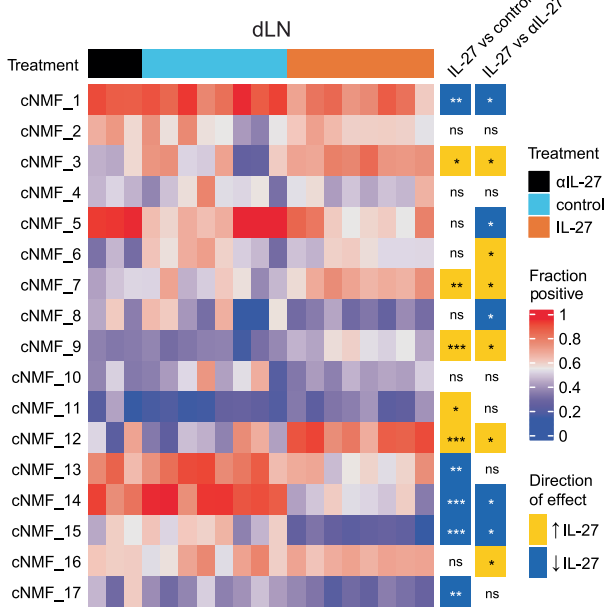
Extended Data Fig. 8 | See next page for caption.

Article

Extended Data Fig. 8 | cNMF profiling of Rpl18-specific CD8⁺ T cells from MC38 tumours and draining lymph nodes. cNMF profiling of pooled T cells from tumour and draining lymph nodes (dLN) revealed 17 programs. Individual cNMF programs were then analysed separately for tumour-infiltrating and dLN-derived T cells. (**a**) UMAP plots showing cNMF program expression intensity across cells (blue, lowest intensity; yellow, highest intensity). (**b**, **c**) Heatmap summarizing average program expression scores (**b**) and fraction of cells with positive program expression (**c**) in samples from individual mice. Samples with fewer than 50 cells were excluded from statistical analysis. P-values are from Wilcox rank-sum test (ns, $P > 0.05$; *$P < 0.05$; **$P \leq 0.01$; ***$P \leq 0.001$; ****$P \leq 0.0001$).

a

OT-1 T cells

day 0 ← IL-27
day 1 ← peptide
day 2 ← IL-27
day 3 ←
day 4 ← IL-27
day 5 ←

IL-27   peptide

b

	TOX	GzmB	SCA-1
0			
0.39			
0.78			
1.56			
3.12			
6.25			
12.5			
25			

IL-27 (ng/ml)

c

SCA-1   TOX   GzmB

control (*n*=3)   IL-27 (*n*=3)

d

GzmB   SCA-1

control   IL-27

Crispr KO: control   IL27RA   control   IL27RA

e

control   IL-27

ECAR (mpH/min) vs Time (minutes)
Glucose, Oligomycin, 2-deoxy-glucose

OCR (pmol/min) vs Time (minutes)
Oligomycin, FCCP, Rotenone + antimycin A

f

MC38-OVA growth (*in vitro*)

Tumour area (normalized to t=0) vs Time (h)

no T cells
OT-I
OT-I treated with IL-27

g

down with IL-27   up with IL-27

Gene set:
CD8 Effector Memory ****
Hypoxia ****
CD8 EarlyActiv ***
Cytotoxic
JAK-STAT *
Trail
p53
CD8 Tex
CD8 NaiveLike
PI3K
WNT
CD8 Tpex
TNFa
VEGF
EGFR
TGFb
NFkB **
MAPK ****

normalized enrichment

h

most increased motifs
most decreased motifs

−log₁₀ (adj. *P*-value) vs log₂ fold change (IL-27 vs control)

Irf1, *Jun*, *Gata3*, *Stat1*, *Tbx21*, *Prdm1*, *Ahr*, *Batf3*

i

Down_IL-27 / Up_IL-27

SP2, E2F4, E2F1, SP3, KLF3, SP1, SP4, KLF1, KLF6, MECP2, ZBT17, KLF5, EGR1, E2F3, NRF1

IRF1, IRF2, IRF7, FOXD3, SRY, STAT2, STAT1, IRF9, IRF8, FOXO4, BATF3, LEF1, PRDM1, FOXL2, IRF4

−log₂ (adj. *P*-value)
0 5 10 15

Fold change
Down Up

j

TF differential expression: −log₁₀ (adj. *P*-value) vs Inferred TF activity: −log₁₀ (adj. *P*-value)

Jun, *Irf1*, *Stat1*, *Tbx21*, *Prdm1*, *Stat2*, *Batf*, *Mef2a*

k

CTL/Treg ratio

control   IL-27-Fc

l

Il27ra^{wt/wt} CD8-cre
Il27ra^{fl/fl} CD8-cre

Tumour volume (mm³) vs Days of treatment

****

m

CD8⁺ T cells

% of CD45⁺ cells

***

Il27ra^{wt/wt} CD8-cre
Il27ra^{fl/fl} CD8-cre

n

CD8⁺ T cells

GzmB (PE-Cy7) vs Rpl18–H-2K^b tet. (PE)

30.6 33.8
14.1
17.6 1.2
4.8

Il27ra^{wt/wt} CD8-cre
Il27ra^{fl/fl} CD8-cre

o

GzmB⁺   Rpl18-specific

% of CD8⁺ T cells

****   ****

Il27ra^{wt/wt} CD8-cre
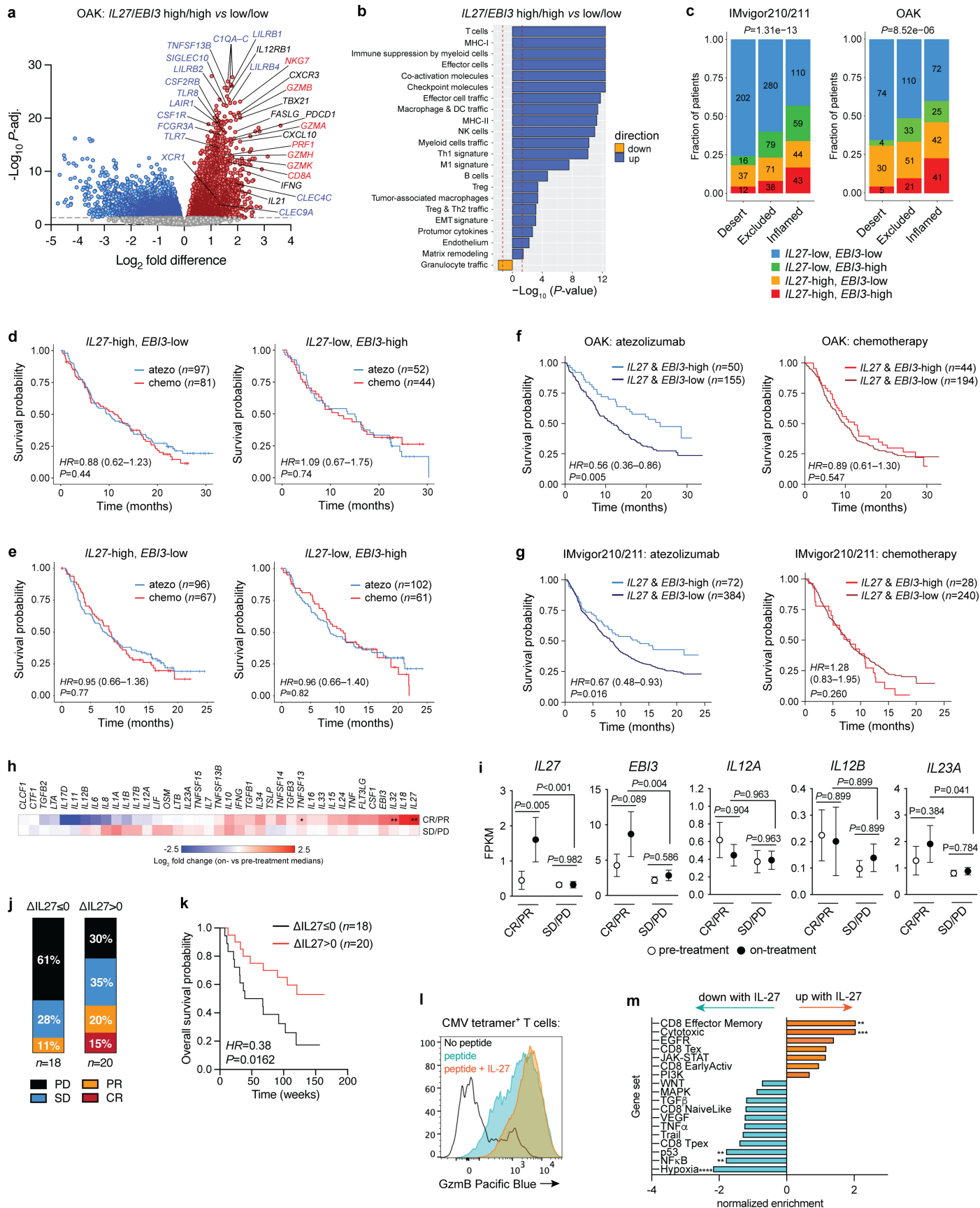*Il27ra^{fl/fl}* CD8-cre

Extended Data Fig. 9 | See next page for caption.

Article

Extended Data Fig. 9 | Cell-intrinsic effects of IL-27 signalling in CD8⁺ T cells.
(**a**–**j**) Analysis of IL-27 effects on CD8⁺ T cell function in an in vitro exhaustion assay. OT-I CD8⁺ T cells were stimulated with SIINFEKL peptide daily ± IL-27. (**a**) Experimental schematic. Cells were evaluated on day 5 in functional assays including flow cytometry (**b**–**d**), metabolic flux (**e**), or target cell killing (**f**). Alternatively, cells were harvested after 4 days for RNAseq and ATACseq (**g**–**j**). (**b**) Normalized z-scores calculated from mean fluorescence intensities of each parameter from $n = 4$ per group. Although biological effects of IL-27 became discernible at approximately 1 ng/ml, the effects were maximal at 25 ng/ml, which was used for all subsequent studies. (**c**) Expression of SCA-1, GzmB, and TOX, compared using two-sided t-test ($n = 2$ per group; *$P < 0.05$, ***$P \leq 0.001$). (**d**) Mean fluorescence intensity of GzmB and SCA-1, averaged from duplicate samples of wild type or IL-27RA CRISPR knockout OT-I cells. Data are representative of 3 independent experiments. Groups compared using two-sided unpaired t-test (ns, not significant; **$P \leq 0.01$). (**e**) Extracellular acidification rate (ECAR) and oxygen consumption rate (OCR) during glycolysis stress test and mitochondrial stress test, respectively. Data represent mean ± s.e.m. of $n = 4$ replicate cultures per group and are representative of two independent experiments. (**f**) OT-I cells co-cultured with OVA-expressing MC38 cells. MC38 proliferation was monitored by live-cell imaging. Data represent two independent experiments. (**g**) RNAseq of OT-I T cells and GSEA analysis of limma-voom differential expression results ($n = 4$ replicate mice per condition) with Benjamini-Hochberg-corrected P-values. *$P < 0.05$, **$P < 0.01$, ***$P < 0.001$, ****$P < 0.0001$. (**h**) Transcription factors (TF) differentially expressed between IL-27-treated versus untreated OT-I cells. Orange data points indicate TF for which predicted DNA binding motifs are strongly enriched in open chromatin regions associated with IL-27 treatment, based on ATACseq analysis (see panel **i**). Conversely, blue data points indicate TFs for which predicted DNA binding motifs are strongly enriched in open chromatin regions associated with control treatment (see panel **i**). (**i**) Motif enrichment analysis of open chromatin regions (based on ATACseq analysis) associated

differentially with IL-27-treated or control conditions. The 15 most strongly enriched TF binding motifs for each condition are shown. (**j**) Inferred activity of transcription factors (x-axis) versus their relative expression under IL-27 treated conditions (y-axis). Inferred activity scores were calculated by first identifying all IL-27-associated open chromatin regions in gene promoters (based on ATACseq) and categorizing them by the presence of TF binding motifs, resulting in candidate gene lists associated with specific transcription factors. These ATACseq derived 'gene sets' were then used for GSEA of the differential gene expression results from the paired RNAseq analysis to determine if genes with open promoters containing specific TF binding sites were also up-regulated by IL-27 treatment. For example, genes with open promoters under IL-27-treated conditions that contained binding sites for STAT1, IRF1, Tbet (*Tbx21*), or Blimp1 (*Prdm1*) were, along with the TFs themselves, highly expressed under IL-27-treated conditions compared to the untreated condition. (**k**) CD8/Treg ratio in MC38 tumour-bearing mice treated with a control antibody or IL-27-Fc ($n = 9$ control, $n = 7$ IL-27-Fc), compared using Mann-Whitney test (*$P = 0.0115$). (**l**–**o**) *Il27ra^{wt/wt}* CD8-cre or *Il27ra^{fl/fl}* CD8-cre mice with established MC38 tumours were treated with 10 mg/kg IL-27-Fc for one week to evaluate whether IL-27-Fc could support anti-tumour CTL responses in the absence of CTL IL27RA expression. (**l**) Tumour growth after initiation of treatment ($n = 24$ *Il27ra^{wt/wt}*, $n = 23$ *Il27ra^{fl/fl}*, pooled from three independent experiments) compared using two-way ANOVA with Holm-Sidak multiple testing correction. ****$P < 0.0001$. (**m**) CTL frequency among tumour-infiltrating CD45⁺ cells. (**n**) Representative staining of Rpl18–H-2K^b tetramer and GzmB in tumour-infiltrating CTL. (**o**) Frequencies of GzmB⁺ and Rpl18-specific cells among tumour-infiltrating CTL. For all bar charts, bars represent mean ± s.e.m. Panels **m**–**o** include $n = 22$ *Il27ra^{wt/wt}* and $n = 16$ *Il27ra^{fl/fl}* mice, pooled from three independent experiments; groups were compared using two-sided Mann-Whitney tests (***$P < 0.001$, ****$P < 0.0001$).

a OAK: *IL27/EBI3* high/high *vs* low/low

b *IL27/EBI3* high/high *vs* low/low

c IMvigor210/211   OAK

d *IL27*-high, *EBI3*-low   *IL27*-low, *EBI3*-high

f OAK: atezolizumab   OAK: chemotherapy

e *IL27*-high, *EBI3*-low   *IL27*-low, *EBI3*-high

g IMvigor210/211: atezolizumab   IMvigor210/211: chemotherapy

h

i *IL27*   *EBI3*   *IL12A*   *IL12B*   *IL23A*

j ΔIL27≤0   ΔIL27>0

k

l CMV tetramer^{+} T cells:

m

Extended Data Fig. 10 | See next page for caption.

Article

Extended Data Fig. 10 | Association of IL-27 expression with immunotherapy response and CTL function in humans. (**a**) Differential gene expression (calculated using Limma-Voom) in NSCLC tumours from the OAK clinical trial, comparing samples with high expression of both *IL27* and *EBI3* versus those with low expression of *IL27* and *EBI3*. Genes highlighted with red text constitute the CTLsig, genes indicated with black text are additional factors relevant to effector T cell responses, and genes highlighted with blue text are related to antigen presenting cells (monocytes, macrophages, and dendritic cells). (**b**) Gene set enrichment analysis to evaluate cellular signatures and their relationship to IL-27 in the OAK dataset. Tumours with high expression of *IL27* and *EBI3* were compared to those with low expression of *IL27* and *EBI3*. (**c**) Association of *IL27* and *EBI3* expression categories with histological tumour immune phenotypes in the IMvigor210/211 and OAK clinical trials. Absolute patient numbers are shown for each immunophenotype and *IL27*/*EBI3* expression category. *P*-values are derived from chi-squared test. (**d**) OS in patients from the OAK trial whose tumours displayed high expression of either *IL27* or *EBI3*. *HR* (and 95% CI) were estimated by a Cox regression model. *P*-values were calculated using the log-rank test. (**e**) OS in patients from the IMvigor210/211 trials whose tumours displayed high expression of either *IL27* or *EBI3*, analysed as in panel **d**. (**f**, **g**) OS of patients with high expression of both *IL27* and *EBI3* vs those with low expression of both *IL27* and *EBI3* within treatment arms of the OAK (**f**) and IMvigor210/211 (**g**) clinical trials. *HR* (and 95% CI) were estimated by a Cox regression model. *P*-values were calculated using the log-rank test. (**h**–**k**) Analysis of therapeutic response to nivolumab (anti-PD-1) and associated changes in tumour cytokine expression in patients with non-ocular melanoma from a previously published dataset of matched pre-treatment and on-treatment biopsies (GSE91061)[48]. (**h**) Fold changes in median cytokine expression in on-treatment *vs* pre-treatment samples in the indicated response groups (CR/PR, *n* = 9; SD/PD, *n* = 29). CR, complete response; PR, partial response; SD, stable disease; PD, progressive disease. *P*-values derived from one-way ANOVA with Holm-Sidak multiple testing correction; *P < 0.05, **P < 0.01. No asterisk, *P* > 0.05. Cytokines with undetectable expression were excluded. (**i**) Mean ± s.e.m. expression of selected cytokines. *P*-values derived from one-way ANOVA with Holm-Sidak multiple testing correction. (**j**, **k**) Patients are separated into two groups based on those whose tumours showed increased *IL27* expression during treatment (relative to pre-treatment biopsies), versus those who showed no change or a reduction in *IL27* expression. (**j**) Clinical responses to nivolumab. (**k**) Kaplan-Meier analysis of OS. *HR* and *P*-value calculated using log-rank test. (**l**, **m**) Bulk primary human CTL (from 3 healthy donors) were engineered to express a CMV-pp65-specific TCR (containing a mixture of CMV-specific and nonspecific cells) and stimulated daily with peptide-loaded target cells ± IL-27 (25 ng/ml). See Fig. 5c for treatment schematic. (**l**) GzmB expression in antigen-specific cells. (**m**) CMV-specific CTL were FACS-purified on day 3 and analysed by RNAseq. Graph summarizes gene set enrichment analysis performed on limma-voom differential expression results. Bar size is proportional to the normalized enrichment score, and stars indicate Benjamini-Hochberg adjusted *P*-values (**P < 0.01, ***P < 0.001, ****P < 0.0001). Data are representative of two independent experiments, each with *n* = 3 independent donors.

nature portfolio

Corresponding author(s): Nathaniel West

Last updated by author(s): Nov 25, 2024

Reporting Summary

Nature Portfolio wishes to improve the reproducibility of the work that we publish. This form provides structure for consistency and transparency in reporting. For further information on Nature Portfolio policies, see our Editorial Policies and the Editorial Policy Checklist.

Statistics

For all statistical analyses, confirm that the following items are present in the figure legend, table legend, main text, or Methods section.

n/a	Confirmed	
☐	☒	The exact sample size (*n*) for each experimental group/condition, given as a discrete number and unit of measurement
☐	☒	A statement on whether measurements were taken from distinct samples or whether the same sample was measured repeatedly
☐	☒	The statistical test(s) used AND whether they are one- or two-sided *Only common tests should be described solely by name; describe more complex techniques in the Methods section.*
☐	☒	A description of all covariates tested
☐	☒	A description of any assumptions or corrections, such as tests of normality and adjustment for multiple comparisons
☐	☒	A full description of the statistical parameters including central tendency (e.g. means) or other basic estimates (e.g. regression coefficient) AND variation (e.g. standard deviation) or associated estimates of uncertainty (e.g. confidence intervals)
☐	☒	For null hypothesis testing, the test statistic (e.g. *F*, *t*, *r*) with confidence intervals, effect sizes, degrees of freedom and *P* value noted *Give P values as exact values whenever suitable.*
☒	☐	For Bayesian analysis, information on the choice of priors and Markov chain Monte Carlo settings
☒	☐	For hierarchical and complex designs, identification of the appropriate level for tests and full reporting of outcomes
☐	☒	Estimates of effect sizes (e.g. Cohen's *d*, Pearson's *r*), indicating how they were calculated

Our web collection on statistics for biologists contains articles on many of the points above.

Software and code

Policy information about availability of computer code

Data collection	Flow cytometry data were collected using BD FACSDiva software. Tumor cell killing was measured using the Incucyte® SX5 Live-Cell Analysis System (Essen Bioscience).
Data analysis	Data analysis was performed with Rstudio (R 4.1.0, Bioconductor 3.13) and GraphPad Prism 8 except when noted otherwise.

For manuscripts utilizing custom algorithms or software that are central to the research but not yet described in published literature, software must be made available to editors and reviewers. We strongly encourage code deposition in a community repository (e.g. GitHub). See the Nature Portfolio guidelines for submitting code & software for further information.

Data

Policy information about availability of data

All manuscripts must include a data availability statement. This statement should provide the following information, where applicable:

- Accession codes, unique identifiers, or web links for publicly available datasets
- A description of any restrictions on data availability
- For clinical datasets or third party data, please ensure that the statement adheres to our policy

The results shown here are in whole or part based upon data generated by the TCGA Research Network: http://cancergenome.nih.gov/. Normalized and batch-adjusted RNA-seq data were obtained from the UCSC Xenabrowser (https://xenabrowser.net/datapages/). Additional publicly available RNAseq datasets used in this study include GSE91061 (nivolumab-treated non-ocular melanoma biopsies), GSE168846 (untreated mouse syngeneic tumours), and GSE199045 (resting mouse

CD8+ T cells). Normalized gene expression data and associated sample metadata were extracted directly from Gene Expression Omnibus (https://www.ncbi.nlm.nih.gov/geo/).

RNAseq data from the IMvigor210, IMvigor211, and OAK studies are available from the European Genome-Phenome Archive (EGA) under accession numbers EGAS00001002556, EGAD00001007703, EGAD00001008391, and EGAS50000000497. Bulk and single-cell raw sequencing data from mouse samples are available from the ArrayExpress database with accession IDs as follows: ATACseq of OT-I T cells (E-MTAB-14584); bulk RNAseq of CD4+ T cells (E-MTAB-14581); bulk RNAseq of OT-I T cells (E-MTAB-14580); scRNAseq (expression) of CD8+ T cells (E-MTAB-14590); scRNAseq (TCR sequencing) of CD8+ T cells (E-MTAB-14601). Bulk sequencing data for human T cells are available from the EGA under accession number EGAS50000000694. No new algorithms were developed for this manuscript. Processed data and analysis code is available through the Open Science Framework (OSF) project with ID f6re4. Biological materials are available upon request from the corresponding author.

Research involving human participants, their data, or biological material

Policy information about studies with [human participants or human data](#). See also policy information about [sex, gender (identity/presentation), and sexual orientation](#) and [race, ethnicity and racism](#).

Reporting on sex and gender	Both males and females were considered in the study design of the IMvigor210, IMvigor211 and OAK trials. Patients of both sexes were enrolled in the trials. The sex information of the patients was collected at the clinics upon the screening of the patients as part of determining their suitability to be enrolled in the trials. Individual-level data cannot be released due to patient consent.
Reporting on race, ethnicity, or other socially relevant groupings	White Caucasians, African Americans, Hispanics and Asians were included in these trials. Patients either self-reported their ethnicity or were reported by the administrative staff by observation during the screening process. To control the confounding variables, we stratified the data with a number of strata during analysis.
Population characteristics	We are presenting data from patients from two indications, including mUC and NSCLC, from three trials: IMvigor210 Phase 2 mUC, IMvigor211 randomized Phase 3 mUC and OAK randomized Phase 3 NSCLC. IMvigor210 was a multicenter, single-arm, phase 2 trial that investigated efficacy and safety of atezolizumab in metastatic urothelial cancer. Cohort 2 of the IMvigor210 trial contained patients who had progressed during or following a prior platinum-based chemotherapy regimen. IMvigor211 was a multicenter, open-label, phase 3 randomized controlled trial contained patients with locally advanced or metastatic urothelial carcinoma after progression with platinum-based chemotherapy. OAK was a randomized, open-label, phase 3 trial contained patients who had squamous or non-squamous non-small-cell lung cancer after receiving one to two previous cytotoxic chemotherapy regimens (one or more platinum based combination therapies).
Recruitment	This information is available for the three trials in previous publications. IMvigor210: https://www.thelancet.com/journals/lancet/article/PIIS0140-6736(16)32455-2/fulltext IMvigor211: https://www.thelancet.com/journals/lancet/article/PIIS0140-6736(17)33297-X/fulltext OAK: https://www.sciencedirect.com/science/article/pii/S014067361632517X
Ethics oversight	N/A (see articles cited above for information on ethics oversight of the original trials)

Note that full information on the approval of the study protocol must also be provided in the manuscript.

Field-specific reporting

Please select the one below that is the best fit for your research. If you are not sure, read the appropriate sections before making your selection.

☒ Life sciences　　　　☐ Behavioural & social sciences　　　　☐ Ecological, evolutionary & environmental sciences

For a reference copy of the document with all sections, see [nature.com/documents/nr-reporting-summary-flat.pdf](#)

Life sciences study design

All studies must disclose on these points even when the disclosure is negative.

Sample size	For pre-clinical and in vitro studies, no sample size calculation was performed. Sample sizes for individual experiments were chosen on the basis of prior experience with specific model systems (e.g. n=10 mice per group in syngeneic tumor growth studies is sufficient to generate statistically meaningful data, given the known mouse-to-mouse variability in tumor control).
Data exclusions	Gene expression datasets: All samples which passed RNA sequencing quality controls were used. No sample exclusion was performed for in vivo or in vitro phenotypic studies.
Replication	Replication was verified in individual biological replicates and studies as detailed in each figure legend.
Randomization	In pre-clinical mouse studies, individual tumor-bearing mice were randomized to different treatment groups with the aid of a custom Excel macro, such that differences in tumor volume variance between groups was minimized.
Blinding	No blinding of experimental groups was performed, as different groups were directly compared for phenotypic differences.

Reporting for specific materials, systems and methods

We require information from authors about some types of materials, experimental systems and methods used in many studies. Here, indicate whether each material, system or method listed is relevant to your study. If you are not sure if a list item applies to your research, read the appropriate section before selecting a response.

Materials & experimental systems

n/a	Involved in the study
☐	☒ Antibodies
☐	☒ Eukaryotic cell lines
☒	☐ Palaeontology and archaeology
☐	☒ Animals and other organisms
☐	☒ Clinical data
☒	☐ Dual use research of concern
☒	☐ Plants

Methods

n/a	Involved in the study
☒	☐ ChIP-seq
☐	☒ Flow cytometry
☒	☐ MRI-based neuroimaging

Antibodies

Antibodies used	Anti-mouse IL-27RA (9527, mIgG2a), anti-mouse PD-L1 (6E11, mIgG2a), anti-mouse IL-27 (4066v10S, mIgG2a), and isotype control mAbs were developed and produced in-house at Genentech using standard hybridoma technology.
	Flow cytometry antibodies (anti-mouse):
	B220-BUV661: clone RA3-6B2; 1/100; BD cat # 612972
	CD3-PE-Cy5.5: clone 145-2C11; 1/100; Biolegend cat # 100310
	CD4-BV786: clone GK1.5; 1/100; Biolegend cat # 100453
	CD4-BUV395: clone GK1.5; 1/100; BD cat # 563790
	CD8-BV711: clone 53-6.7; 1/100; Biolegend cat # 100759
	CD8-BUV737: clone 53-6.7; 1/100; BD cat # 612759
	CD8-BB515: clone 53-6.7; 1/100; BD cat # 564422
	CD8-FITC: clone KT15; 1/100; Thermo Fisher cat # MA5-16759
	CD8-PE: clone 53-6.7; 1/100; Biolegend cat # 100708
	CD11b-af700; clone M1/70; Biolegend cat # 101222
	CD39-PE-Cy7; clone Duha59; 1/50; Biolegend cat # 143806
	CD39-af647; clone Duha59; 1/50; Biolegend cat # 143808
	CD45-BV510; clone 30-F11; 1/200; Biolegend cat # 103138
	CD45-PE-Cy5.5; clone 30-F11; 1/200; eBioscience cat # 35-0451-80
	CD45.1-BUV737; clone A20; 1/200; BD cat # 612811
	CD45.1-af488; clone A20; 1/200; Biolegend cat # 110717
	CD45.2-BV711; clone 104; 1/100; Biolegend cat # 109847
	CD45.2-PE; clone 104; 1/200; Biolegend cat # 109808
	CD45.2-PE-Dazzle-594; clone 104; 1/200; Biolegend cat # 109846
	Foxp3-ef450; clone FJK-16s; 1/100; eBioscience cat # 48-5773-82
	GzmA-APC; clone GzA-3G8.5; 1/100; eBioscience cat # 17-5831-82
	IFNg-PE-Dazzle-594; clone XMG1.2; 1/200; Biolegend cat # 505846
	IL-10-BV421; clone JES5-16E3; 1/200; Biolegend cat # 505022
	IL-10-af647; clone JES5-16E3; 1/200; Biolegend cat # 505014
	Ki67-af700; clone 16A8; 1/200; Biolegend cat # 652420
	Ly6C-af647; clone HK1.4; 1/200; Biolegend cat # 128010
	PD1-BV786; clone 29F.1A12; 1/100; Biolegend cat # 135225
	PD1-PE-Dazzle-594; clone RMP1-30; 1/200; Biolegend cat # 109116
	PD-L1-BV421; clone MIH5; 1/100; BD cat # 564716
	Sca1-BV711; clone D7; 1/200; Biolegend cat # 108131
	Thy1.2-BUV805; clone 53-2.1; 1/100; BD cat # 741908
	Thy1.2-af700; clone 53-2.1; 1/100; Biolegend cat # 140324
	TNF-BV711; clone MP6-XT22; 1/100; Biolegend cat # 506349
	Flow cytometry antibodies (anti-mouse/human):
	GzmB-PacBlue; clone GB11; 1/100; Biolegend cat # 515408
	GzmB-PE-Cy7; clone QA16A02; 1/20; Biolegend cat # 372214
	TOX-PE; clone REA473; 1/50; Miltenyi cat # 130-120-716
	Flow cytometry antibodies (anti-human):
	CD8-BV510; clone RPA-T8; 5 ul/test; Biolegend cat # 301048
	CD19-BV785; clone SJ25C1; 5 ul/test; BD cat # 563325
	CD20-BUV395; clone L27; 1/40; BD cat # 740204
	TIGIT-APC; clone 741182; 1/40; R&D Systems cat # FAB7898A
Validation	Commercially available flow cytometry antibodies used in this study are extensively validated in the literature, and validation data are

Validation	available on manufacturers' websites.

Anti-mouse IL-27RA was used for flow cytometry and its specificity was confirmed using murine CRISPR knockout cell lines. Anti-mouse PD-L1 blocking antibody has been reported previously (e.g. Huseni et al, Cell Rep Med, 2023; Oh et al, Nat Cancer, 2020); its specificity in our studies was confirmed by its ability to prevent staining with anti-PD-L1 flow cytometry antibodies that bind to overlapping epitopes. Anti-mouse IL-27 neutralizing antibody performance was validated using an in vivo IL-27 challenge assay (see Extended Data Fig. 3a).

Eukaryotic cell lines

Policy information about cell lines and Sex and Gender in Research

Cell line source(s)	The MC38 cell line was obtained from the University of Leiden, Netherlands. The E0771 cell line was purchased from CH3 Biosystems. The B16-F10 cell line was obtained from American Type Culture Collection (ATCC; Manassas, VA).
Authentication	Cell lines were authenticated by RNAseq
Mycoplasma contamination	Cell lines are routinely screened and cells used in studies described in this manuscript were negative for mycoplasma. Two methods of mycoplasma detection were used to avoid false positive/negative results: Lonza Mycoalert and Stratagene Mycosensor.
Commonly misidentified lines (See ICLAC register)	N/A

Animals and other research organisms

Policy information about studies involving animals; ARRIVE guidelines recommended for reporting animal research, and Sex and Gender in Research

Laboratory animals	Female mice aged 6-12 weeks of age were used for pre-clinical experiments. All mice were from a C57BL/6 genetic background. Strains used in this manuscript: CD45.2+ C57BL/6J (Jackson Labs stock #000664) CD45.1+ C57BL/6J Jackson Labs stock #002014) Ebi3–/– (Jackson Labs stock #008691) Rag2–/– (Taconic stock RAGN12, or Jackson Labs stock #008449) C57BL/6J OT-I TCR-transgenic (Jackson Labs stock #003831) Il27ra–/– (generated and bred at Genentech) Il27ra.loxp (generated and bred at Genentech) Il27p28.loxp (generated and bred at Genentech) E8i.Cd8.Cre (Jackson Labs stock #008766) LysM.Cre (Jackson Labs stock #004781) Clec9a.Cre (Jackson Labs stock #025523) Foxp3-GFP (Jackson Labs stock # 006772)
Wild animals	This study did not include wild animals.
Reporting on sex	Only female mice were used for pre-clinical studies, since it is not practical to randomize male mice into co-housed treatment groups (due to fighting between non-littermate males).
Field-collected samples	This study did not involve samples collected from the field.
Ethics oversight	Animal studies were approved by Genentech's Institutional Animal Care and Use Committee and adhered to the NRC Guidelines for the Care and Use of Laboratory Animals.

Note that full information on the approval of the study protocol must also be provided in the manuscript.

Clinical data

Policy information about clinical studies

All manuscripts should comply with the ICMJE guidelines for publication of clinical research and a completed CONSORT checklist must be included with all submissions.

Clinical trial registration	IMvigor210 (NCT02108652); IMvigor211 (NCT02302807); OAK (NCT02008227)
Study protocol	IMvigor210--Previously published in: Rosenberg, J. E. et al. Atezolizumab in patients with locally advanced and metastatic urothelial carcinoma who have progressed following treatment with platinum-based chemotherapy: a single-arm, multicentre, phase 2 trial. Lancet 387, 1909–1920 (2016). IMvigor211--Previously published in: Powles, T. et al. Atezolizumab versus chemotherapy in patients with platinum-treated locally advanced or metastatic urothelial carcinoma (IMvigor211): a multicentre, open-label, phase 3 randomised controlled trial. Lancet 391, 748–757 (2018).

OAK--Previously published in:
Rittmeyer, A. et al. Atezolizumab versus docetaxel in patients with previously treated non-small-cell lung cancer (OAK): a phase 3, open-label, multicentre randomised controlled trial. Lancet 389, 255–265 (2017).

Data collection | Data collection is described in the references provided above.

Outcomes | Clinical outcome measures are described in the references provided above.

Flow Cytometry

Plots

Confirm that:

☒ The axis labels state the marker and fluorochrome used (e.g. CD4-FITC).

☒ The axis scales are clearly visible. Include numbers along axes only for bottom left plot of group (a 'group' is an analysis of identical markers).

☒ All plots are contour plots with outliers or pseudocolor plots.

☒ A numerical value for number of cells or percentage (with statistics) is provided.

Methodology

Sample preparation | See Methods: Tissue preparation and flow cytometry

Instrument | See Methods: Tissue preparation and flow cytometry

Software | See Methods: Tissue preparation and flow cytometry

Cell population abundance | For FACS-sorting experiments, post-sort purities were routinely above 98% based on flow cytometry analysis of post-sort versus pre-sort samples.

Gating strategy | A general gating strategy for T cell identification and analysis is provided in Extended Data Fig. 10.

☒ Tick this box to confirm that a figure exemplifying the gating strategy is provided in the Supplementary Information.